ACS APPLIED MATERIALS & INTERFACES

www.acsami.org

Review

Emerging Trends in Additive Manufacturing for Thermoelectric Devices: Materials, Structures, and Engineering Approaches

R S Kondaguli,[†] Inder Kumar,[†] C R Hiremath, P V Malaji, Somashekara Makireddypalli Adinarayanappa, and Ramesh Chandra Mallik*

Cite This: https://doi.org/10.1021/acsami.6c04499

Read Online

ACCESS | Metrics & More | Article Recommendations

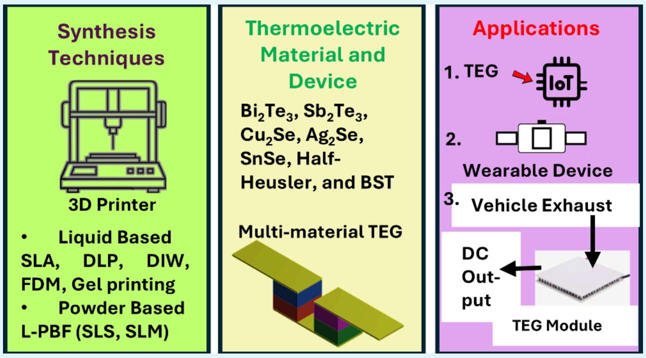

ABSTRACT: Energy harvesting is gaining importance in the 21st century, with thermoelectric (TE) technology offering a promising method for converting thermal energy into electrical energy. However, the application of TE devices remains relatively low because of the limitations of conventional manufacturing methods. Fabricating complex-shaped TE devices using traditional manufacturing processes is challenging and leads to a low efficiency. Unlike conventional subtractive methods, additive manufacturing (AM) builds three-dimensional (3D) objects layer by layer, enabling the creation of intricate and complex structures with precision. This study explores recent trends in AM of thermoelectric systems, with a focus on materials, synthesis methods, and device fabrication. It also discusses the challenges associated with these AM techniques and explores potential areas for improvement. Recent studies have shown that AM can produce thermoelectric units with hollow and layered structures, enhancing temperature gradients and power density compared with conventional designs. The ability to customize geometries through AM offers promising opportunities to enhance the performance of the TE materials and devices. AM technologies can produce highly efficient, functionally graded TE devices. By enabling rapid prototyping and high-performance structures, AM can improve the efficiency and application of the TE materials. Future work focuses on further advancing these AM techniques by integration with machine learning (ML) and development of multimaterial TE devices.

KEYWORDS: *additive manufacturing, thermoelectric materials, 3D printing, thermoelectric devices, sustainable energy, direct ink writing*

1. INTRODUCTION

1.1. Global Energy Context

The global demand for energy has increased significantly with advancements in technology.[1,2] In the 21st century, energy harvesting has become important due to the focus on sustainability, energy efficiency, and technological advances.[1,2] The fulfillment of energy demands cannot be achieved by fuel cells as fuel sources are limited despite their high efficiency (50−60%).[3] To meet the energy demand, photovoltaic cells (PVs)[4] and thermophotovoltaic (TPV) devices[5,6] play a crucial role, as they convert sunlight and thermal radiation, respectively, into electrical energy. However, a significant amount of unused energy exists as waste heat generated by automobiles, households, industries, and the human body. Thermoelectric generators (TEGs) directly convert waste heat into electricity, making them solutions for waste-heat recovery. TEG modules have a lifetime of approximately 23 years with minimal maintenance.[7] In practical applications, TEGs have been integrated into automotive exhaust systems and industrial boilers for harvesting waste heat. A 40-module TEG integrated with an IC engine exhaust produced ~25 W at ~1.56% efficiency.[8] Similarly, in large industrial facilities, TEGs are deployed to capture heat from furnace walls. On smaller scales, miniature TEGs harvest heat from CPUs, sensors, or even human skin. TEGs are increasingly used in Internet of Things (IoT) devices, sensor networks, and wearable systems as autonomous power sources.[9,10] Since they require only small temperature differences (ΔT), body heat or low thermal gradients are sufficient to power low-energy sensors and circuits. A flexible wearable TEG with a power circuit powered Bluetooth at a skin-air temperature difference of 4 K.[11] Wearable and microscale TEGs give continuous energy but low power (<0.1 mW/cm^2), while industrial TEGs produce higher power (~10−100 mW/cm^2). TEGs are used in space as radioisotope generators to power spacecraft and in the military

Received: March 4, 2026
Revised: May 13, 2026
Accepted: May 13, 2026

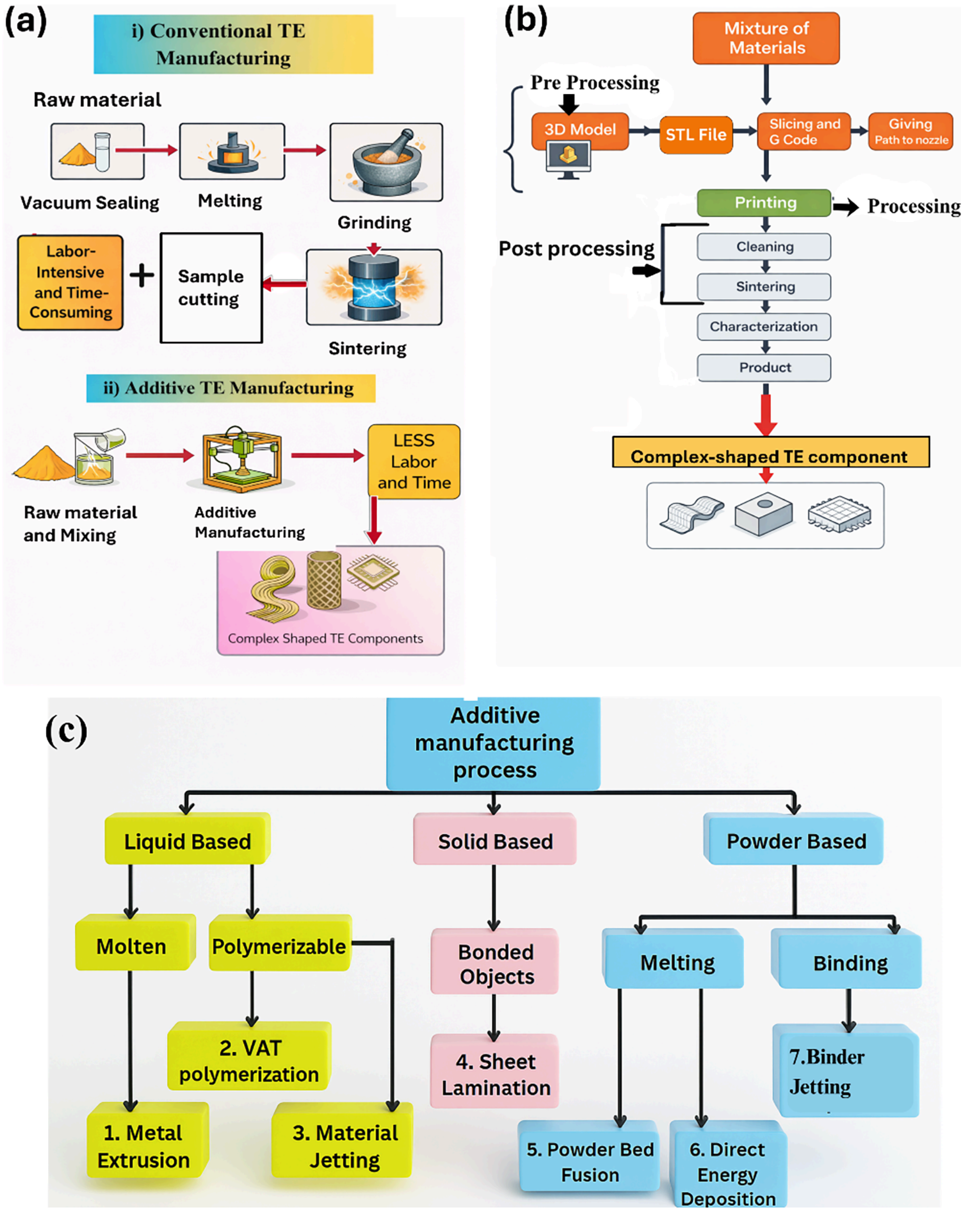

Figure 1. (a) Comparison of thermoelectric material manufacturing approaches: (i) conventional manufacturing, which includes the steps of melting, grinding, sintering, and sample cutting and (ii) additive manufacturing, which shows the fabrication of complex-shaped material and is less time-consuming.[24] (b) Schematic workflow for additive manufacturing starts with the sample preparation, followed by the processing step and finally the postprocessing step.[25] (c) Overview of the ASTM-Classified Additive Manufacturing technologies based on the liquid, solid, and powder.[26] (created using Canva).

as silent energy sources for surveillance sensors and soldier equipment. TEGs exhibit comparatively lower conversion efficiencies (8−11% at 300−1300 K)[12−15] as compared to the PV cell (15−27% at 233−358 K)[16,17] and TPV cell (30−40% at 1273−2673 K).[5,6] However, TEGs offer advantages such as compactness, modular scalability, and reliability and its ability to recover waste heat. These properties enable TEGs to function as complementary energy-conversion technologies rather than competitors to other clean-energy systems.

1.2. Thermoelectricity

Thermoelectric devices enable direct conversion between heat and electricity through two principles: the Seebeck and Peltier effects. According to the Seebeck effect, when a temperature gradient is applied across the junction of two dissimilar materials, an electric voltage is generated. The generated voltage depends on the material's Seebeck coefficient (S) and the applied temperature gradient, and it is given as[18]

$$S = -\lim_{\Delta T \to 0} \frac{\Delta V}{\Delta T} \tag{1}$$

where ΔV is the potential gradient and ΔT denotes the temperature gradient. The S is the Seebeck coefficient, which is a material property and depends on the carrier concentration and the energy-dependent mobility of the charge carriers. The thermoelectric generator operates on the Seebeck effect.

The Peltier effect is the reverse of the Seebeck effect. In the Peltier effect, when an electric current passes through the junction of two dissimilar materials, one end absorbs heat and the other releases it, depending on the current direction. The current direction and magnitude applied to the junction

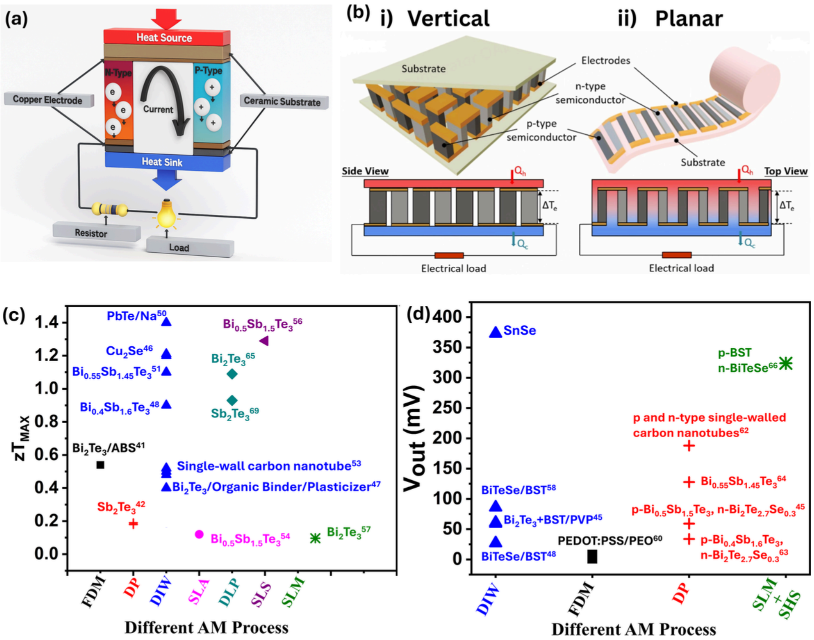

Figure 2. (a) Schematic of thermoelectric generators (TEGs) showing the components such as the p- and n-type legs and the contact materials. The TEGs operate when connected to a heat source and sink (created using Canva). (b) Different topologies of TEGs: (i) vertical, (ii) planar.[30] Reproduced with permission from ref 30 Copyright 2023 ACS Energy Letters. (c,d) Maximum *zT* and output voltage of thermoelectric materials and devices fabricated using various additive manufacturing techniques.

determine the amount of heat released or absorbed at the junction, and it can be described as[18]

$$\dot{Q} = \Pi_{AB} I \tag{2}$$

where $\dot{Q}$ denotes the time rate of heat energy evolved or absorbed and Π_{AB} represents the relative Peltier coefficient. The thermoelectric refrigerator works on the principle of the Peltier effect.

The performance of a thermoelectric material depends on the dimensionless figure of merit, zT, as expressed in eq 3:[18]

$$zT = \frac{S^2\sigma}{\kappa} T \tag{3}$$

Here, S represents the Seebeck coefficient, σ denotes the electrical conductivity, T signifies the absolute temperature, and κ corresponds to the thermal conductivity.

A wide range of materials, including Bi_2Te_3, PbTe, SnSe, Cu_2Se, GeTe, and Half-Heuslers, exhibit thermoelectric performance across different temperature regimes. Bi_2Te_3 remains efficient near room temperature (300−500 K) with zT ~1.2,[19] while midtemperature materials such as SnSe and GeTe achieve higher performance (zT ~3.1 for SnSe and ~2.3 for GeTe).[20,21] At high temperatures (>900 K), materials such as SiGe and NbFeSb-based Half-Heuslers demonstrate stable performance (zT >1).[22]

For the TEG, the maximum conversion efficiency can be written as[23]

$$\eta_{\max} = \frac{\Delta T}{T_H} \frac{(1 + <ZT>)^{1/2} - 1}{(1 + <ZT>)^{1/2} + T_C/T_H} \tag{4}$$

where <ZT> represents the average thermoelectric figure of merit of the device.

However, traditional fabrication methods (melt spinning, spark plasma sintering, arc melting, and ball milling) are high-energy processes that result in material waste (in the dicing step). A schematic of the thermoelectric material synthesis and device fabrication process is shown in Figure 1a(i). Figure 1a shows that the conventional approach is labor-intensive and time-consuming, requiring multiple processing stages. Additionally, they are limited to planar configurations, which restrict efficient heat transfer on curved surfaces due to elevated thermal resistance.[27] Hence, there is a growing need for fabrication techniques that enable conformal geometries and improved device integration. Figure 1a(ii) illustrates that unlike traditional subtractive techniques, AM constructs objects layer by layer, adding material until the final geometry is achieved. This approach is particularly advantageous for designing complex, multimaterial, embedded, customized, and ready-to-use thermoelectric components. Additionally, it reduces thermal resistance, which, in turn, enhances overall efficiency.

1.3. Additive Manufacturing (AM)

Additive manufacturing is a set of processes that construct three-dimensional objects by sequentially depositing material in layers, continuously guided by computer-aided-design (CAD) models.

Figure 1b shows the workflow for the AM of TE materials, which starts with a parametric CAD model that is exported to a printable file format. The stereolithography (STL) file encodes only a triangular surface mesh.[28] This STL file is divided into several layers, which is called slicing. The sliced model is then translated into G-code, providing instructions for the AM system to construct the part. After fabrication, the component is termed a green part. It is a printed component with its intended shape but not fully consolidated due to residual binders, solvents, or loosely packed powders. Such an early-stage component remains mechanically weak and requires postprocessing to improve its strength. Not all AM techniques produce green parts; binder-based, unsintered processes form green bodies, whereas melt-based methods do not. It is then

Table 1. Thermoelectric Figure of Merit (zT), Seebeck Coefficient (S), Electrical Conductivity (σ), and Thermal Conductivity (κ) of the Different Materials Synthesized by the AM Process

material	T (K)	σ (S/cm)	S (μV/K)	κ (W/m K)	zT	Process
BST(81.3%)/MWCNTs(4%)/PLA	300	3.54	179 (p-type)	0.31	0.011	FDM[40]
Bi_2Te_3/(80%) ABS	300	54.6	240 (p-type)	0.17	0.54	FDM[41]
Sb_2Te_3/epoxy	300	60	160 (p-type)	0.24	0.19	DP[42]
$Pb_x(Bi_{0.5}Sb_{1.5})_{1-x}Te_3$, x = 0.0025	300	6.5	220 (p-type)	0.25	0.045	DIW[43]
	363	9.5	260 (p-type)		0.08	
CB/BTBA/PLA	300	13.1	125 (p-type)	0.28	0.024	DIW[44]
Bi_2Te_3	300	104	−112 (n-type)	0.53	0.11	DIW[45]
Cu_2Se-based	300	900	50 (p-type)	0.6	0.12	DIW[46]
	1000	180	190 (p-type)	0.5	1.21	
Bi_2Te_3/organic binder/plasticizer	323	780	−90 (n-type)	0.75	0.33	DIW[47]
$Bi_{0.4}Sb_{1.6}Te_3$	300	550	166 (p-type)	0.63	0.8	DIW[48]
$Bi_{0.55}Sb_{1.45}Te_3$ /ChaM wt.10%	300−500	650	180 (p-type)	0.9	0.85	DIW[49]
$Pb_{0.98}Na_{0.02}Te$	300	2000	50 (p-type)	3	0.1	DIW[50]
	800	350	240 (p-type)	0.98	1.4	
$Bi_{0.55}Sb_{1.45}Te_3$	300	600	200 (p-type)	0.78	0.95	DIW[51]
	400	450	210 (p-type)	0.72	1.1	
BTNW	300	700	−110 (n-type)	1.3	0.2	DIW[52]
	463	400	−125 (n-type)	1.2	0.3	
SWCNT	303	370	−28 (n-type)	0.13	0.1	DIW[53]
	453	470	−40 (n-type)	0.07	0.48	
$Bi_{0.5}Sb_{1.5}Te_3$	300	50	148 (p-type)	0.48	0.12	SLA[54]
Bi_2Te_3	300	360	−128 (n-type)	0.24	0.74	DLP[55]
	500	432	−120 (n-type)	0.29	1.09	
$Bi_{0.5}Sb_{1.5}Te_3$	300	480	168 (p-type)	0.3	1.15	SLS[56]
Bi_2Te_3	323	250	180 (p-type)	0.8	0.11	SLM[57]

subjected to subsequent processing steps, such as support structure elimination, surface cleaning, and thermal treatment to attain the desired surface finish and material properties.[29]

As depicted in Figure 1c, the AM technique is categorized into three types based on the starting material: solid, liquid, and powder states. Furthermore, according to the ISO/ASTM 52900:2015 standard, AM techniques are divided into seven categories: material extrusion, powder bed fusion (PBF), directed energy deposition (DED), material jetting (MJ), binder jetting, vat photopolymerization (VAT), and sheet lamination (SL).

Figure 2a represents the TEG, which is composed of p-type and n-type semiconductors arranged with thermal connections in parallel and electrical connections in series. TE devices are primarily categorized into two basic architectures: the vertical configuration and the planar or lateral thermopile layout, as illustrated in Figure 2b. In a vertical TEG,[31] the thermocouples are aligned vertically, following the direction of heat flow from the hot to the cold side, normal to the substrate, as shown in Figure 2b(i). AM manufacturing techniques, such as fused deposition modeling (FDM), stereolithography (SLA), selective laser sintering (SLS), selective laser melting (SLM), and binder jetting,[32] are typically used to prepare these types of TEGs. Planar TEGs, on the other hand, have thermocouples deposited on a substrate in the direction of lateral heat flow, as shown in Figure 2b(ii). Unlike vertical designs, planar configurations offer greater fabrication flexibility and are adaptable to various substrates, including integrated circuits, flexible materials, and curved surfaces.[33] These planar TE devices are fabricated using methods such as direct ink writing (DIW), material jetting,[30] aerosol jetting,[34] and inkjet printing.[35]

Recent reviews highlight the application of AM in thermoelectrics. Zhang et al. emphasized the DIW-based fabrication for the flexible TE devices and nanostructuring strategies.[36] Bi et al. presented a broad review of AM-processed TE materials, detailing the processing parameters that affect material quality and transport properties and summarizing the capabilities of each AM method for device fabrication.[37] Rani et al. offered an overview of AM techniques, their early demonstrations, and the challenges encountered in applying them to TE materials and devices.[38] Baroutaji et al. provided a comprehensive overview of thermoelectric fundamentals, materials, and AM techniques, including powder- and extrusion-based methods. The review highlights key challenges, including porosity, processing complexity, and post-treatment requirements as well as limitations in current AM technologies for TE applications.[39]

In contrast, the present review provides a more integrated and analytical perspective by systematically correlating process−structure−property relationships across different AM techniques. This review further highlights hybrid fabrication strategies, emerging approaches such as machine-learning-assisted optimization, and functionally graded TE systems. These aspects have received less attention in previous reviews, making this work a more comprehensive framework for understanding and advancing AM-enabled thermoelectric technologies.

The thermoelectric performance of various TE materials and devices fabricated using AM methods is illustrated in Figure 2c,d, respectively, which will be discussed in detail in the following sections. The thermoelectric characteristics and device performance of these materials are presented in Tables 1 and 2, respectively.

Table 2. Thermoelectric Device Performance (Power Output and Voltage Output) of the Different Materials Synthesized by the AM Process

material	V_{out} (mV)	Power (μW)	ΔT (K)	TE Legs (pairs)	process
BiTeSe/BST	86.1	187,000	224.96		DIW[58]
reduced graphene oxide (rGO)	12		80		[59]
PEDOT:PSS/PEO	1.3	46	128		FDM[60]
PEDOT:PSS/DMSO	4.3	0.012	32	10	DP[61]
p-$Bi_{0.5}Sb_{1.5}Te_3$/PVP	59.21	23.97	60.8	5	DP[45]
n-$Bi_2Te_{2.7}Se_{0.3}$/PVP					
p-SWCNT/PAA	188.08	1.68	20	140	DP[62]
n-SWCNT/PEI					
p-$Bi_{0.4}Sb_{1.6}Te_3$	33.9	4.44	20.9	10-pair	DP[63]
n-$Bi_2Se_{0.3}Te_{2.7}$					
$Bi_2Te_{2.7}Se_{0.3}$/PLG	8	0.026	10	5-pair	FDM[43]
$Bi_{0.5}Sb_{1.5}Te_3$/PLG					
$Bi_{0.55}Sb_{1.45}Te_3$	127.9	0.49	40	10-pair	DP[64]
SnSe	373	145	251		[65]
Bi_2Te_3 (vertical)		0.003		5	DIW[43]
Bi_2Te_3 and BST (annular)/PVP	60.8	678	54.6	5	DIW[45]
Bi_2Te_3 and BST (planar)/PVP	59.21	23.97	60.8	5	DIW[45]
BST/BiTeSe (half annular)	27	1620	39	3	DIW[48]
p-type Sb_2Te_3 coating n-type Bi_2Te_3 coating		3.2	120		DLP[55]
p-BST n-BiTeSe	324	4970	40	28	SHS/SLM[66]

2. SYNTHESIS OF THERMOELECTRIC COMPONENTS VIA ADDITIVE MANUFACTURING TECHNIQUES

In recent studies, AM has been used to create thermoelectric units with various geometries including hollow and layered structures.[49,67] These geometries exhibit significant improvements in performance compared to conventional cuboid designs.[68,69] Specifically, units with hollow or layered geometries show temperature gradients that are 35 to 55% higher in aerial power density. This advancement is associated with the ability of AM to produce intricate internal structures that enhance the thermal and electrical performance.

Currently, several 3D printing processes are available for modern additive manufacturing. In this work, these are classified based on the state of the material during additive manufacturing such as liquid or powder.

2.1. Liquid-Based Additive Manufacturing

Liquid additive manufacturing (LAM) processes employ materials in the liquid state during printing. These are explained in detail in the following section.

2.1.1. VAT Photopolymerization. Photopolymerization-based LAM processes fabricate objects by curing a photocurable liquid resin under UV light exposure. The UV light selectively scans each cross section of the slice and cures only the required part. Once a layer is fully cured, the build platform moves down or up, and a successive layer of liquid resin spreads over or beneath the previous layer, which is then cured again. This layer-by-layer process continues until the entire object is built. Finally, the uncured resin is drained from the vat, and the object is processed. The schematic of VAT photopolymerization is shown in Figure 3a.

VAT polymerization has two types, namely, stereolithography (SLA) and digital light processing (DLP), based on the curing method. The primary difference between DLP and SLA is that the DLP technique uses a projected light source to cure the layer. However, in SLA, a laser is used that cures the resin along the path. These are explained in the following subsections.

2.1.1.1. Stereolithography (SLA). This concept was initially introduced by Chuck Hull.[71] He et al.[54] investigated the AM of amorphous p-type $Bi_{0.5}Sb_{1.5}Te_3$ (BST) using photocurable composite resins. The SLA-based resin curing performed in a layer-by-layer enabled the fabrication of high-loading thermoelectric materials (40−60 wt % BST). This SLA-mimicked process is illustrated in Figure 3b. The κ for the 50 wt % BST with 1.5 h annealing shows a similar value (~0.2 W/m K) over the temperature range of 50−300 K, which is due to the amorphous behavior of the material. For the 60 wt % BST, the grain sizes increased from ~46 to 68 nm with increasing annealing time, and a zT of 0.12 was achieved at 316 K after annealing for 6 h, due to improved electrical conductivity. However, samples exhibit high porosities (60−70%), which suppress the electrical conductivity, and result in low zT (0.12 at 316 K) compared to the hot-pressed BST (1.2 at 300 K).[72]

Mallick et al.[73] reported that SLA-based 3D scaffolds coated with n-type Ag_2Se achieved a zT of about 1 at room temperature. This good performance was due to the high electrical conductivity (~472 S/cm) and large Seebeck coefficient (~−183 μV/K). This is attributed to improved phase formation and grain connectivity induced during printing and sintering. The TEG is fabricated using the n-type Ag_2Se and commercially available p-type poly(3,4-ethylenedioxythiophene) (PEDOT). Despite PEDOT having a low zT (~ 10^{-2}), the devices achieve power outputs of ~0.4 μW for a cuboid module and up to 7 μW at ΔT = 70 K for a cylindrical design, with a cold side temperature of 293 K. Although the thermal contact resistance, high internal resistance, and a reduced effective temperature gradient restrict the performance (up to 15%), the important study is the reproducibility and stability of the device after 16 cycles for 32 h. Overall, the work demonstrates that Ag_2Se can be integrated into TEGs, with further advances in the development of improved printable p-type materials and the implementation of automated multimaterial printing for scalability.

Tiwari et al.[74] explored a hybrid approach that combines hot-pressing and stereolithography techniques. The Sb_2Te_3 powder was filled into a 3D-printed mold and compacted under different temperatures (373 and 473 K) and compressive forces (500 or 1000 N). The polymer mold was later eliminated following the sintering process, resulting in the formation of the final TE components. When the compressive force is 500 N at 573 K, the electrical conductivity increased for the sintered sample (1.4 S/cm) as compared to the nonsintered sample (0.76 S/cm). This increase is attributed to densification and reduced porosity during pressing and sintering, which improved carrier transport. This report highlights that higher temperatures and forces led to a higher density and a more uniform microstructure, which enhances electrical conductivity. However, this approach still faces limitations such as residual porosity, contamination from the mold, and additional postprocessing steps, which hinder

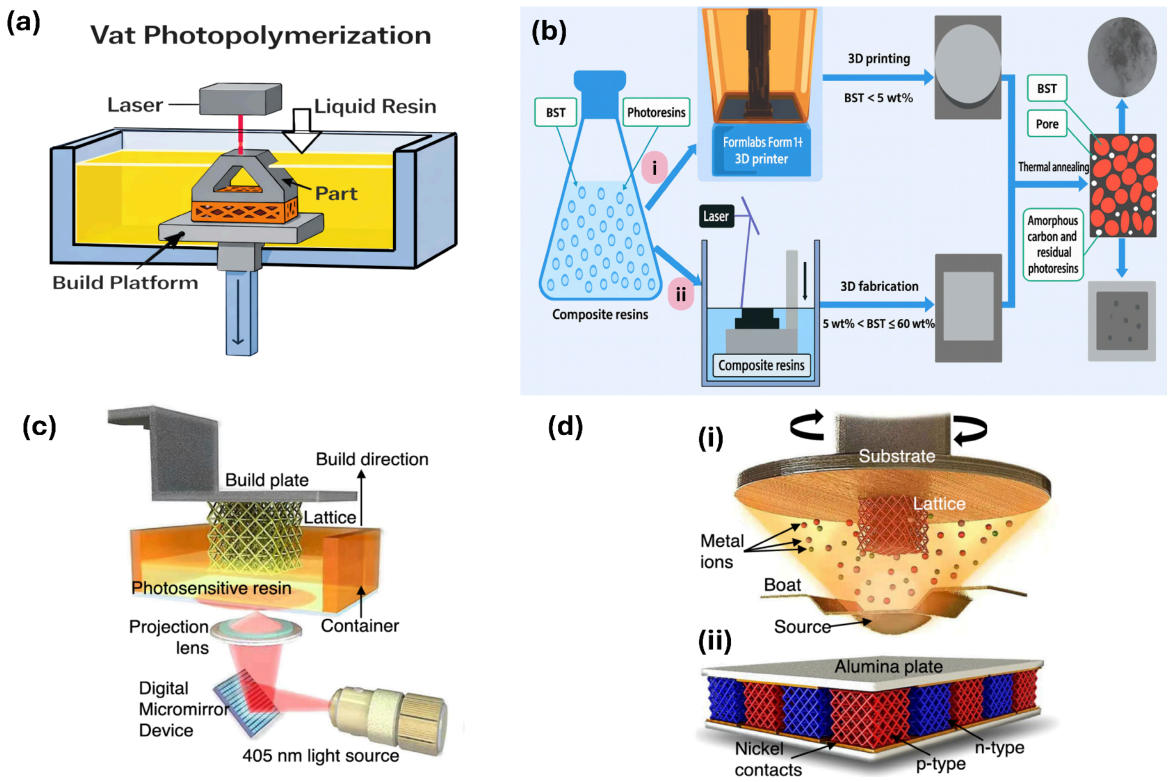

Figure 3. (a) Block diagram of the VAT photopolymerization process[70] (created using Canva). (b) Schematic pathways for (i) additive manufacturing and (ii) three-dimensional structuring of $Bi_{0.5}Sb_{1.5}Te_3$ specimens, blended with tailored photopolymer resins, succeeded by heat treatment.[54] Reproduced with permission from ref 54 Copyright (2015), (John Wiley & Sons - Books). (c) Schematic illustrating the DLP method employed for fabricating polymeric microlattices. Reproduced with permission from ref 55 Copyright (2023), (Nature Publishing Group). (d) Schematic representations of DLP fabrication, (i) thermal evaporation on substrate, (ii) TEG with p- and n-type material.[55] Reproduced with permission from ref 55 Copyright (2023), (Nature Publishing Group).

scalability and prevent achieving high thermoelectric performance.

The additional challenges in SLA include the choice of resin for resin preparation and the curing process, which can affect the consistency and properties of the final product. This additive manufacturing method has a limitation: it requires the use of a support material, resulting in material waste. Though SLA is a slow-printing method, it has the advantage of high resolution (∼10 μm), which results in high-quality structures.[75,76]

2.1.1.2. Digital Light Processing (DLP). DLP operates by utilizing an arrangement of microscopic mirrors to redirect ultraviolet (UV) light. When light is incident on these mirrors, it is reflected onto a substrate. In the presence of liquid resin, redirected UV light solidifies it. TE composites were prepared by Park et al.[77] employing DLP, using a UV-sensitive resin system containing diurethane dimethacrylate (DUDMA) and isobornyl acrylate (IBOA) as the matrix, with Ag_2Se serving as the filler. The fabrication process involved varying Ag_2Se concentrations (0, 10, 20, and 30 wt %) to evaluate mechanical and thermoelectric characteristics. The thermogravimetric analysis (TGA) results show that the cured photo resin undergoes weight loss at approximately 600 K. The tensile strength of these samples with varying Ag_2Se filler contents ranges from 16.7 to 40.3 MPa. The incorporation of Ag_2Se improves electrical transport and introduces multiple interfaces, which enhance phonon scattering and reduce thermal conductivity. The reported zT value is 0.12 at 300 K for 30% Ag_2Se, which remains significantly lower than bulk thermoelectric materials (zT ∼1). Despite the low zT, this report provides a key concept for fabricating TE composites using the DLP technique.

Karthikeyan et al.[55] introduce a methodology to enhance the energy-conversion efficiency and mechanical strength of TEGs by utilizing three-dimensional microlattice architectures. As shown in Figure 3c,d, DLP is used to fabricate polymeric microlattices, followed by partial carbonization and coating with p-Sb_2Te_3 and n-Bi_2Te_3. The resultant core−shell microlattices exhibited high compressive strength (∼450 MPa) and deformability, with a specific energy uptake approaching 30 J/g and an energy-conversion efficiency of nearly 10%. This improvement arises from the cellular architecture, which enhances thermal gradients and reduces effective thermal conductivity while maintaining mechanical robustness. These outcomes underline the potential of 3D microlattice configurations in enhancing TEG performance and reliability. A limitation lies in the complexity of manufacturing such structures, which may hinder scalability for widespread implementation. The challenge for DLP is to develop the resin. The modification in the resin involves nanoparticle doping and a carbon additive that can enhance the power factor and lower the thermal conductivity.[78]

2.1.2. Material Extrusion (ME). Material extrusion encompasses two main methodologies: FDM and DIW.

2.1.2.1. The Fused Deposition Method (FDM). FDM is one of the most common AM techniques utilized for fabricating models, prototypes, and functional components. This technique is known for its rapidity, straightforwardness, and

https://doi.org/10.1021/acsami.6c04499
ACS Appl. Mater. Interfaces XXXX, XXX, XXX−XXX

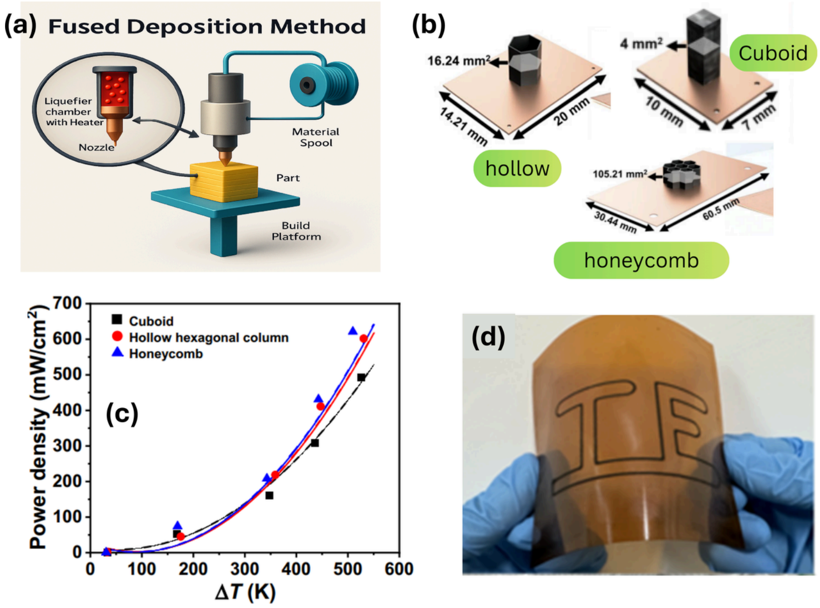

Figure 4. (a) Schematic diagram of the fused deposition method (created using Canva). (b) Illustration of DIW printing different 3D filling techniques,[46] reproduced with permission from ref 46 Copyright 2021 Nature Communications. (c) Power by different 3D filling techniques,[46] reproduced with permission from ref 46 Copyright 2021 Nature Communications. (d) 2D pattern-printed design with flexibility (postcuring).[64] Reproduced with permission from ref 64 Copyright 2024 American Chemical Society.

cost-efficiency. This method was developed in the late 1980s by S. Scott Crump and was introduced commercially in 1990.[79] Currently, FDM or fused filament fabrication (FFF) continues to dominate the global 3D-printing landscape. Nevertheless, limited work has been done on exploring the fabrication of thermoelectric materials with an FDM. This process operates by extruding a thermoplastic filament through a heated nozzle, as illustrated in Figure 4a. However, manufacturing a thermoplastic filament that incorporates thermoelectric elements poses challenges. Researchers have addressed these issues by combining thermoplastics such as polylactic acid (PLA) and acrylonitrile butadiene styrene (ABS) with TE constituents to produce functional filaments.[40,80] PLA is widely used in FDM due to its nontoxicity and excellent strength.

Wang et al.[40] were the first to investigate FDM with PLA/$Bi_{0.5}Sb_{1.5}Te_3$ composite filaments enhanced with multiwalled carbon nanotubes (MWCNTs) for 3D printing. The silane coupling agent KH570 is added to enhance the adhesion between PLA and BST, enabling the actual BST loading to closely match the designed composition. The addition of the saline coupling agent KH570 considerably increased BST loadings to 73.1 and 79.7% for the designed loadings of 75 and 80%, respectively. The composite with 87.5 wt % BST achieved a zT of 0.006 at room temperature. By introducing the 4 wt % MWCNTs and 81.3 wt % BST, the composite filaments exhibited a zT of 0.011 at room temperature. These advancements are attributed to the improved dispersion of BST and the inclusion of the MWCNTs. This work presents useful material-processing results for improving PLA/BST composite filaments for FDM printing. However, the thermoelectric performance is low, and characterizations such as porosity, microstructure, and device-level testing are missing. Overall, FDM offers advantages in scalability and low-cost fabrication. However, insulating polymer binders, porosity, and weak interfacial transport limit its thermoelectric performance, requiring binder-free or postprocessing strategies.

Aw et al.[81] investigated the influence of infill percentage on the mechanical and thermoelectric behaviors of conductive acrylonitrile butadiene styrene with zinc oxide (CABS/ZnO) composites fabricated using FDM. Two infilling patterns, such as line and rectilinear, are studied. For 100% infill density, the maximum Young's modulus is 1.3 GPa. For a CABS line filling of 100%, the zT value reported is 5.7×10^{-5} at room temperature. The study systematically links FDM infill density and printing pattern to mechanical and thermoelectric behavior in CABS/ZnO composites. However, despite improved mechanical properties, the thermoelectric performance remains low due to the dominance of the insulating polymer matrix, which limits charge carrier transport. The absence of microstructural analysis and the low zT values ($\sim 10^{-5}$) limit the significance and practical relevance of the work.

The study by Ozatn et al.[41] examines the application of FFF for the production of thermoelectric materials. The process involved creating composite filaments from Bi_2Te_3 and ABS, followed by 3D printing and sintering of the samples. The samples' sintering is required to remove the polymer and fuse the Bi_2Te_3 material, thereby increasing the electrical conductivity. To remove the polymer, a sufficiently high temperature is required, below the material's melting point. For this case, the sufficient temperature for the removal of the polymer is above 450 K. It is observed that the electrical conductivity of the sintered sample is three times higher than that of the unsintered sample. A zT of 0.54 at room temperature is reported for a sample sintered at 773 K, although it still lags behind conventional bulk manufacturing methods in terms of overall efficiency. The complex structures (concentric circles and star) fabricated in this work highlight the capability of FFF to produce complex and nonconventional geometries that are difficult to achieve using traditional processing routes. For instance, the cylindrical structure design is important for curved surfaces, such as pipes, where heat harvesting from radial temperature gradients is required.

Similarly, nonlinear geometries, such as the star-shaped design, demonstrate the potential for device architectures to enhance heat exchange and surface area. Such complex geometries provide opportunities to optimize thermal gradients, improve heat-transfer efficiency, and design applications for thermoelectric devices. Future work should focus on establishing quantitative relationships between geometry and thermoelectric performance, particularly regarding the heat flow distribution and transport properties.

Yu et al.[82] reported the development of a volume-metallized 3D-printed polymer composite (VMPC) by infusing low-melting-point metal (LM) into the porous configuration of ABS. This bicontinuous phase is developed by FDM technology, which exhibits improved mechanical strength and electrical and thermal performance. The tensile strength of VMPC is 35.41 MPa, with high electrical conductivity ($>10^4$ S/cm) and thermal conductivity of 25.29 W/(m K). VMPC does not act as a thermoelectric material. It serves as a multifunctional thermal-management and conductive medium that maximizes the temperature difference applied across a TEG. The VMPC acted as an efficient thermal-management scaffold when coupled with a thermoelectric generator, stabilizing a temperature difference of ∼30 K and enabling power generation of $\approx 300 \times 10^3$ μW. This methodology explores the potential of the AM technique for improving heat harvesting in thermoelectric systems.

Since the FDM process operates at 473 K, there is a potential risk of oxidation in FDM-printed thermoelectric materials. Oxidation poses a significant challenge, as it can degrade both the mechanical integrity and the thermoelectric performance of these materials. Oxides are brittle and prone to cracking, leading to potential mechanical failure during operation.[83] Implementing a protective atmosphere during the FDM process could effectively reduce oxidation. Another challenge in using FDM for TE materials is the low electrical conductivity of the filaments, which is attributed to the high polymer content.[36] These polymers can be removed by sintering the material below its melting point under an inert atmosphere.[41] Otherwise, the FDM is a low-cost technique with a resolution of ∼50 to 200 μm.[75]

2.1.2.2. Direct Ink Writing (DIW). DIW is an AM technique that utilizes a slurry of conductive thermoelectric powders and polymers acting as binders and dispersants.[84] In recent years, this method has emerged as an effective approach to processing functional materials. It enables the fabrication of multimaterial structures and the creation of complex, free-standing structures suitable for flexible and wearable applications.

Ink design for DIW is generally built on three key strategies. The first strategy focuses on optimizing the slurry composition, where the proportions of TE powders, binders, and dispersants are tuned to achieve a uniform ink. The second strategy adjusts the physical properties of the ink, particularly viscosity, yield stress, and shear thinning behavior, ensuring that the ink extrudes easily but quickly regains strength to hold its printed shape. The third strategy involves printing of complex, application-specific thermoelectric architectures.

Chen et al.[42] developed dispenser-printed flat TEGs using Bi_2Te_3 and Sb_2Te_3 composite inks. These devices showed zT values of 0.18 (n-type) and 0.19 (p-type) at room temperature. The inks were made by mixing 80−82% Bi_2Te_3 or Sb_2Te_3 powder with 18−20% epoxy resin as a binder. A 50-couple device generated a power output of 10.5 μW and a voltage of 171.6 mV under a temperature difference of 20 K.. However, the polymer binder and interfacial resistance limit electrical conductivity, resulting in high device resistance (2.55 kΩ) and reduced performance. This makes the printed composite method useful mainly for very low-power uses. Adding conductive materials like graphene, reduced graphene oxide (rGO), carbon nanotubes (CNTs), or silver nanowires can also improve conductivity. Using low-temperature sintering can further improve particle connections without damaging the polymer, lowering internal resistance and improving charge flow. Together, these steps can increase the overall efficiency of the device.

Choo et al.[46] utilized extrusion-based printing for Cu_2Se thermoelectric architectures as shown in Figure 4b,c, achieving a zT of 1.21 at 1000 K. The study presents an approach combining the extrusion-based 3D printing with a cellular honeycomb structure for Cu_2Se. A power density of 621.40 mW/cm^2, mechanical robustness (modulus 0.93 GPa), with a 3-fold increase in fracture strain was observed. The rheological tuning using Se_8^{2-} polyanions is effective, enabling stable printing and uniform TE properties across multiple geometries (cuboid, hollow, hexagonal column, and cellular honeycomb). Cellular architectures (hexagonal and honeycomb) exhibit improved generation efficiencies of ∼7.3 and ∼7.7% at 873 K, representing ∼22−26% enhancement over conventional cuboid geometries.[46] This improvement arises from reduced lateral heat spreading and more uniform temperature distribution at the electrode interfaces, enabling efficient heat utilization. These results highlight the critical role of geometry in optimizing device-level thermoelectric performance. However, the work also exhibits some challenges. The zT improvement remains low compared to traditional fabricated Cu_2Se, where the reported zT value is 3.3.[85] The reduction in κ to 0.5 W/m K is largely due to porosity, and challenges arise from dimensional accuracy issues resulting from sintering shrinkage of 60−70%. Additionally, only p-type Cu_2Se is demonstrated, which limits the practical integration of devices due to the absence of a high-performance n-type counterpart. Overall, the study demonstrates device design and good mechanical performance.

Cui et al.[64] demonstrated the advancement of 3D-printed Bi_2Te_3-based TEGs. The thermoelectric ink, composed of Bi_2Te_3 particles and glycerol in a weight ratio of 1:0.7, was 3D printed and sintered at 573, 623, and 673 K. At a sintering temperature of 623 K, the printed devices exhibited a Seebeck coefficient of 288 μV/K and a power factor of 0.042 μW/m K^2 at room temperature. This improvement arises from optimized sintering at 623 K, which enhances particle crystallization, leading to higher electrical conductivity and power factor. These devices, shown in Figure 4d, generated an output voltage of 127.94 mV at a ΔT of 40 K, demonstrating potential in energy harvesting and temperature sensing. These printed TEGs are flexible, enabling use in complex, customizable shapes, broadening their potential for home-scale and industrial applications.

Yang et al.[51] fabricated a compositionally segmented $Bi_xSb_{2-x}Te_3$ ($x = 0.3-0.6$) multimaterial. This enables control over peak zT from 300 to 523 K while maintaining good compatibility among the segments. The incorporation of $Sb_2Te_4^{2-}$ chalcogenidometallate binder provides viscoelasticity. The 3D-printed objects were sintered at 723 K, resulting in crack-free interfaces and minimal electrical or thermal losses, which yield an efficiency of 8.7% at $\Delta T = 236$ K. However, the

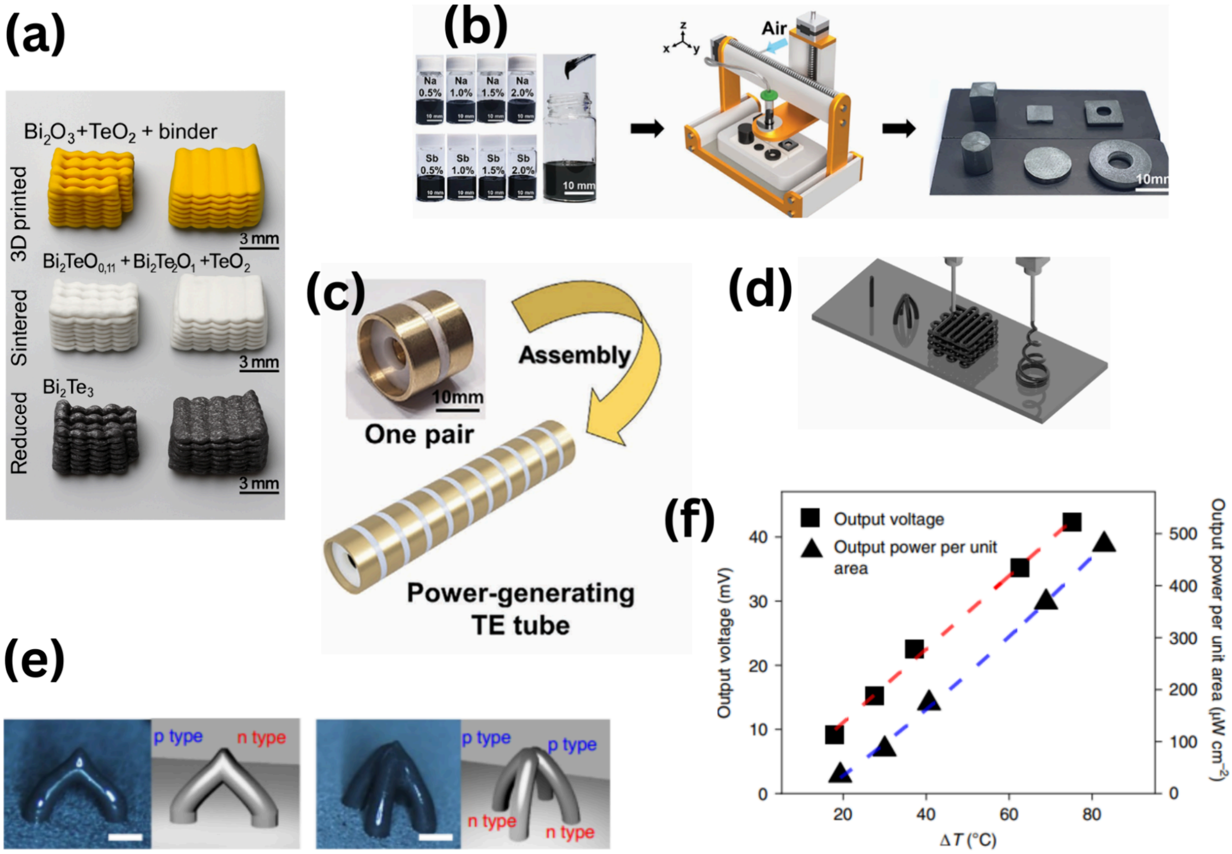

Figure 5. Illustration of direct ink writing and its applications: (a) printed Bi_2O_3 and TeO_2 green bodies, air presintered ceramic phases comprising $Bi_2Te_4O_{11}$ with $Bi_2Te_2O_7$ and TeO_2 and coreduced Bi_2Te_3 thermoelectric materials, showing microlattice (left) and dense (right) configurations;[47] reproduced with permission from ref 47 Copyright 2021 PERGAMON. (b) Bulk PbTe samples in different geometries, subsequently utilized to develop an operational thermoelectric generator.[50] (c) Power-generating tube;[50] reproduced with permission from ref 50 Copyright 2021 John Wiley & Sons – Books. (d) Direct ink writing process.[49] (e) Charge-coupled device (CCD) imagery and illustrated arch-shaped configurations of interconnected p-type and n-type TE legs; scale bars: 500 μm.[49] (f) Power output by μTEG through direct 3D ink printing.[49] Reproduced with permission from ref 49 Copyright 2021 Nature Electronics.

printed samples exhibit 20–25% porosity, which reduces electrical conductivity, and the demonstration is limited to a single p-type leg rather than a full p-n module. Additionally, long-term reliability shrinkage mismatch issues appear when binder content varies. Despite these limitations, the work significantly advances TE manufacturing by offering a scalable, cost-effective strategy for fabricating high-performance segmented TEGs.

Kenel et al.[47] investigated the ink extrusion of Bi_2Te_3, achieving a zT value of 0.4 at 373 K. The parts are shown in Figure 5a. This study demonstrates the formation of Bi_2Te_3 through oxide-based 3D printing, supported by in situ synchrotron XRD. However, the low relative density (~50%) limits densification and thermoelectric performance, as porosity increases phonon scattering but also hinders electrical transport due to poor carrier pathways. Lee et al.[50] developed PbTe-based TE inks, demonstrating enhanced viscoelasticity and power generation in tubular TEGs. The 3D-printed parts are shown in Figure 5b,c, where individual p-n tubular pairs are laterally integrated to form a power-generating TE tube. The work demonstrates doping-induced viscoelasticity, enabling the 3D printing of PbTe with high zT values (1.4 for p-type at 700 K and 1.2 for n-type at 750 K) and very low thermal conductivities (0.80 W/m K for p-type and 0.65 W/m K for n-type). This arises from doping-induced carrier optimization and porosity-driven phonon scattering, which together enhance thermoelectric performance. This tubular architecture allows direct integration with heat sources such as exhaust systems and improves heat-transfer efficiency. This work reported an output voltage of 83.2 mV at a temperature difference of 300 K.

Kim et al.[49] formulated viscoelastic TE inks of $(Bi,Sb)_2(Te,Se)_3$ with chalcogenidometalates. This enables direct 3D writing of intricate microarchitectures with zT values of 1 for p-type materials and 0.5 for n-type materials at 350 K. The printed parts are shown in Figure 5d–f. The work showed that DIW can create thermoelectric structures with a good performance. This is enabled by a controlled particle size, surface oxidation, and binder-free ink design. However, its dependence on specific sintering conditions, porosity effects, and short cooling durability limits its practical use. To address these challenges, future efforts should focus on improving densification through higher solid loading, controlled particle size distribution, and optimized sintering strategies.

Zhang et al.[52] explored the fabrication of Bi_2Te_3-based nanowire ink via a solvothermal method, washed, and dispersed it in an ethanol–ethylene glycol mixture. The ink was then 3D-printed using DIW, where shear thinning properties facilitated nanowire alignment. Annealing at 673 K in a hydrogen atmosphere enhanced the thermoelectric properties, yielding an electrical conductivity of 450 S/cm and a reported zT value of 0.31 at 433 K.

https://doi.org/10.1021/acsami.6c04499

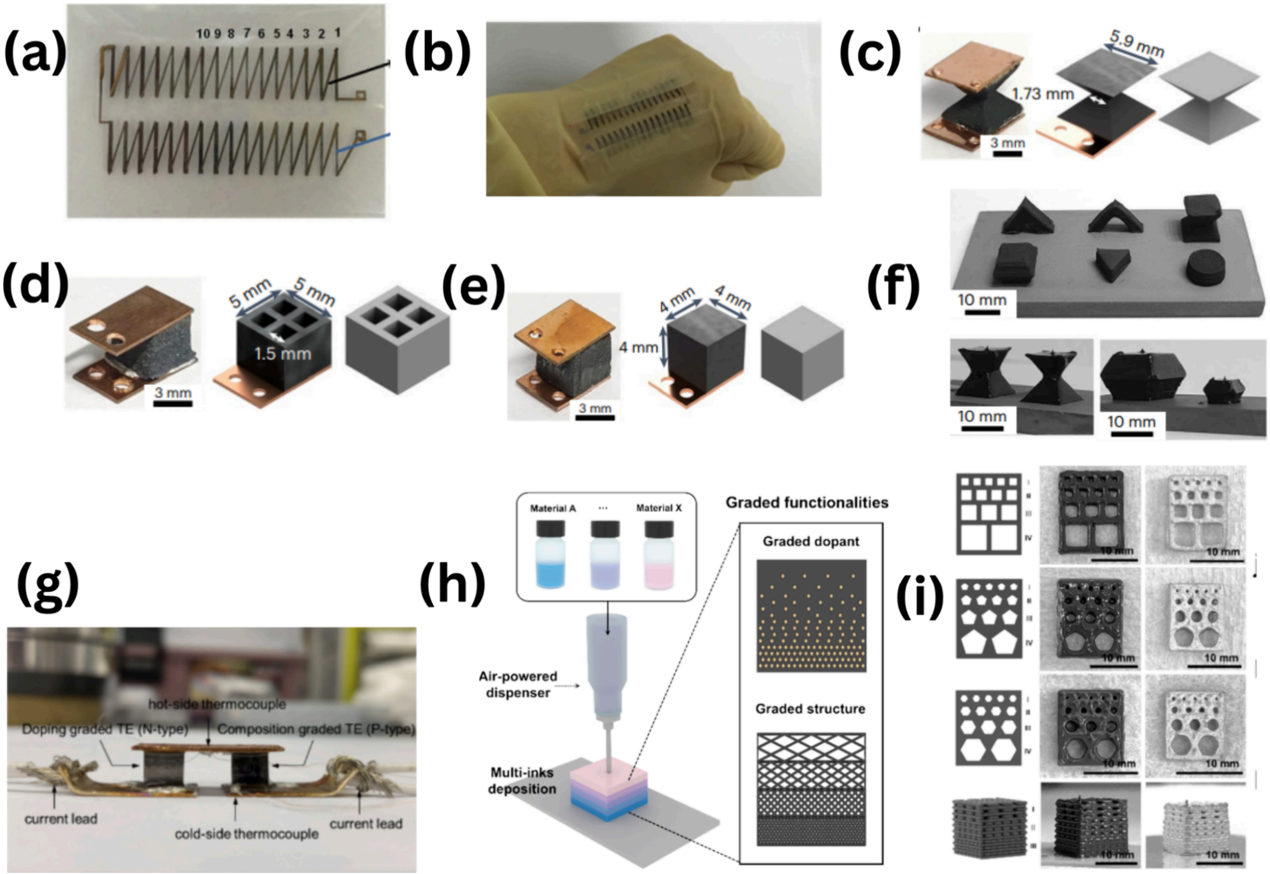

Figure 6. Various thermoelectric devices and structures fabricated using additive manufacturing: (a,b) Planar TEGs,[86] reproduced with permission from ref 86 Copyright 2016 Scientific Report. (c–e) 3D models of TE devices.[87] (f) Free-standing shapes of Cu_2Se printed using entirely inorganic Cu_2Se ink,[87] reproduced with permission from ref 87 Copyright 2024, Nature Energy. (g) 3D-printed functionally graded thermoelectric module.[58] (h) Diagram of the extrusion-based AM technique for producing dopant-graded and void-graded functionally graded thermoelectric modules,[58] and (i) structural void-graded thermoelectric module with different void geometries.[58] Reproduced with permission from ref 58 Copyright 2024, Chemical Engineering Journal.

Bae et al.[86] enhanced poly(3,4-ethylenedioxythiophene)/poly(styrenesulfonate) (PEDOT:PSS) and tellurium-PEDOT:PSS composites via sulfuric acid treatment, significantly improving electrical conductivity. The electrical conductivity value increased from 787.99 to 4839.92 S/cm for PEDOT:PSS and from 11.01 to 334.68 S/cm for Te-PEDOT:PSS. Although the Seebeck coefficient decreased, power factors reached 0.051 mW/m K^2 for PEDOT:PSS and 0.284 mW/m K^2 for Te-PEDOT:PSS at room temperature.

A flexible TEG (Figure 6a,b) fabricated from treated Te-PEDOT:PSS generated a voltage of 2 mV and a maximum power output of 10.59 nW. These fabricated devices are suitable for wearable electronics. Choo et al. introduced a geometric design strategy for Cu_2Se-based TE materials (Figure 6c–f).[87] Various 3D-printed shapes, including cuboids and hourglass structures, were optimized via FEM simulations, evaluating the temperature difference, electrical resistance, and output power. The hourglass design exhibited superior performance, generating 2.1 times more power and 3.6 times greater efficiency than the cuboids at 873 K. This improvement is attributed to geometry-induced enhancement in thermal resistance and temperature gradient while maintaining lower electrical resistance due to larger contact areas, thereby improving power output. Notably, this geometry enables tuning of the ratio of electrical to thermal current density, thereby overcoming the intrinsic trade-off between the electrical and thermal transport.

Han et al.[58] developed functionally graded thermoelectric materials (FGMs) using 3D printing (Figure 6g,h,i). To make the viscous ink, the thermoelectric powder and $Sb_2Te_4^{2-}$ were mixed with glycerol. To fabricate a TEG, n-type $Bi_2Te_{2.7}Se_{0.3}$ legs with a Na-dopant gradient were combined with a p-type $Bi_yTe_{2-y}Se_{0.3}$ leg carrying a controlled composition gradient. The Na-doped sintered sample shows no impurity peak in the XRD, confirming phase purity. The SEM image revealed that grain sizes ranged from a few micrometers to several tens of micrometers. They attained a maximum power density of 357 mW/cm^2, marking a 20% improvement over homogeneous materials. Haile et al.[88] developed a double Half-Heusler material with the composition $Ti_{1.75}Zr_{0.25}Ni_{1.5}Fe_{0.5}SnSb$ and used DIW to print thermoelectric legs in various geometries (solid, mesh, hollow, and honeycomb structures). Among all the designs, the honeycomb geometry exhibited the highest efficiency, showing an improvement of approximately 25.6% compared to the solid geometry. Malki et al.[89] reported the 3D ink printing of $Nb_{1-x}CoSb$, where the printed sample exhibited a zT of ∼0.1 at 873 K, which is lower compared to the conventional sintered counterpart that achieved a zT of 0.7–0.9.[89,90]

DIW is highly suited for TE materials because it avoids high-temperature energy input that may cause volatile element loss

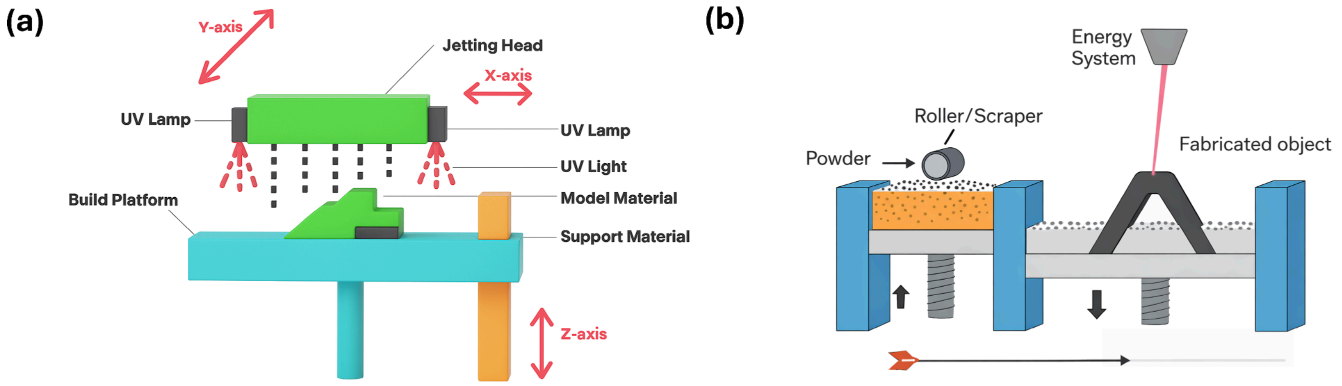

Figure 7. (a) Schematic diagram of material jetting[70] and (b) block diagram illustrating powder bed fusion.[70] (Created using Canva).

(e.g., Sb, Bi, S, and Te). It is cost-effective and industrially scalable. Despite these advancements, DIW-fabricated parts often suffer from low-dimensional accuracy and geometric defects, with shrinkage during curing leading to warping. To address these challenges, future efforts focus on improving ink rheology, increasing solid loading, and optimizing sintering protocols to minimize shrinkage and enhance structural stability. Such advancements are required for achieving reliable, high-performance thermoelectric devices and translating DIW from laboratory-scale demonstrations to practical applications.

2.1.3. Material Jetting (MJ). Material jetting (MJ) is an additive manufacturing technique that produces layered components by curing numerous tiny photopolymer droplets with UV light, as shown in Figure 7a. In practice, the process begins with heating a liquid photopolymer resin to obtain a viscosity that the printing head can handle. The liquid resin is subsequently ejected as hundreds of tiny droplets from the print head and cured using an integrated UV light source, delivering a smooth surface finish. MJ includes a range of individual methods, such as drop-on-demand (DoD), inkjet printing, nanoparticle jetting (NPJ), PolyJet,[91] and aerosol jetting.[92] Aerosol jetting is mainly used in the field of electronic material deposition.

Juntunen et al.[93] developed graphene-based organic nanocomposites using a scalable inkjet printing technique. The graphene ink was formulated by ultrasonically exfoliating graphite crystals in isopropyl alcohol. The different concentrations of polyvinylpyrrolidone (PVP) (3, 6, 12, and 24 mg) were used to optimize viscosity and surface tension for stable and precise DoD printing. The printed films exhibited a disordered nanoporous structure that acts as a phonon-glass electron-crystal behavior. This arises from a 3D network of few-layer graphene flakes, where interflake interfaces suppress thermal transport while maintaining electrical conduction. This results in a room-temperature power factor of 0.019 mW/m K^2, marking a 3-fold improvement over the previous solution-processed graphene structure. Furthermore, flexible thermoelectric devices comprising multiple graphene legs interconnected with inkjet-printed silver were fabricated on Kapton polyimide substrates. They showed excellent mechanical durability over 10,000 bending cycles. The device shows a linear voltage response with increasing temperature difference. This highlights the promise of inkjet-printed graphene thermoelectric devices for flexible and wearable use. Inkjet-printed graphene films show promise for flexible energy harvesting, although their low zT of $\sim 10^{-3}$ still limits real-world impact. Besganz et al.[94] explored inkjet-printed thermoelectric composites (PEDOT:PSS/ZnO), achieving 9.1 mV potential difference at $\Delta T = 100$ K and 11.1×10^{-3} μW power at optimal ZnO concentrations (PEDOT:PSS-ZnO$_{0.2}$).

This method enables an excellent surface finish and is ideal for visual or prototype evaluations. Its primary drawback is material degradation under prolonged light or UV exposure due to photopolymerization, limiting its suitability for functional TE applications. Aerogel printing is a subset of material jetting; the next section extends the discussion to gel- and aerogel-based printing approaches.

2.1.3.1. Gel and Aerogel Printing Approaches. Recent advancements in additive manufacturing have enabled several fabrication strategies for thermoelectric materials through gel- and aerogel-based printing approaches. Aerogels, invented in 1931 by Kistler, represent an ultralight class of solids containing up to 95% air, characterized by a highly interconnected nanoscale network and open porosity.[95] These structures are formed by replacing the solvent within wet-gel precursors with air without collapsing the porous framework. This results in an ultralow thermal conductivity (0.010 W/m K). Consequently, aerogels show strong potential for flexible TE applications that require efficient heat management.

Ou et al.[96] explored the enhancement of thermoelectric properties in flexible nanocomposites by utilizing aerosol-jet printing. In this work, MWCNTs and Sb_2Te_3 nanoflakes are incorporated in a PEDOT:PSS matrix. The materials were printed onto flexible polyimide substrates. This technique enabled the in situ mixing of the components, resulting in a uniform dispersion of the mixture. These high-conductivity MWCNTs and high-Seebeck coefficient Sb_2Te_3 nanoflakes enhance electrical transport. An optimal loading fraction of 85 wt % yielded a power factor of 41×10^{-3} mW/m K^2, which is among the highest reported for printed organic-based thermoelectric materials. The flexibility and robustness of these materials were measured for 36,000 cycles. The resistance of these nanocomposites did not return to its original value after releasing due to the formation of small cracks. This work demonstrates the potential of using such nanocomposites for flexible thermoelectric energy harvesting applications. However, the thermal conductivity measurement was not provided, which lacks the result in calculating the zT.

Weinbach et al.[97] reported the 3D printing of a PEDOT:PSS aerogel with extreme porosity (93%). This material exhibits a Seebeck coefficient of ~ 18 μV/K and a thermal conductivity of ~ 0.065 W/m K, yielding a zT of 2.7×10^{-3} at 300 K. Sun et al. successfully reported CNT/Ag aerogels with a very low density

(0.13 g/cm^3), where Ag nanoparticles enhance electrical conductivity while the porous framework reduces thermal transport. The reported zT is 0.011 at 300 K.[97] Zhang et al.[98] developed an in situ porous TEG heat-harvesting model using porous thermoelectric materials. A gyroid-structured $Bi_{0.5}Sb_{0.5}Te_3$ material was fabricated via DIW. This 3D-printed $Bi_{0.5}Sb_{0.5}Te_3$ enables efficient heat flow without hindering exhaust dynamics. Conventional TEGs typically capture heat from exterior surfaces. However, this technique has the potential to extract maximum heat directly from the source. The porous $Bi_{0.5}Sb_{0.5}Te_3$ exhibits a zT value of 0.187 at 423 K with an effective electrical conductivity of 15 S/cm and a low thermal conductivity of 0.087 W/(m K).

Zeng et al. introduce a printing method called high-throughput combinatorial printing (HTCP). In this, different nanomaterial inks are turned into tiny aerosol droplets, mixed inside a single nozzle using airflow, and deposited as very thin films with fine control (~20 μm resolution and ~100 nm thickness).[99] The method works with many materials, including metals like silver, thermoelectric compounds such as Bi_2Te_3, polymers like PEDOT:PSS, MXenes, and oxides, showing strong flexibility. The results are impressive, with high thermoelectric power factor (~1774 μW/m K^2) in sulfur-doped $Bi_2Te_{2.7}Se_{0.3}$, the created polymer films with stiffness changing over a wide range and demonstrating controlled chemical changes like GO to rGO.[99] Overall, the technique allows fast screening of many material combinations and offers clear advantages over traditional methods like sputtering or inkjet printing. However, there are limitations: the composition gradients are not linear and printed films have lower electrical performance due to diluted inks and need extra processing. Additionally, there are issues like jet instability and nozzle clogging. Also, the method has only been tested on small-scale samples, so its large-scale manufacturing potential is not yet proven.

Overall, PEDOT:PSS aerogels offer low κ but exhibit low TE performance (zT ~10^{-3}). CNT/Ag aerogels provide enhanced conductivity but remain fragile, achieving zT ~0.01, whereas Bi_2Te_3 aerogels deliver zT ~0.1−0.5 while maintaining low κ.

2.2. Powder-Based Additive Manufacturing

Powder-based additive manufacturing incorporates a powder material during the printing process. These are explained in the following section.

2.2.1. Powder Bed Fusion. Powder bed fusion employs a laser or electron beam as an energy source to selectively melt the powdered material at specific locations, which subsequently undergoes solidification layer by layer. This process utilizes powdered raw materials, as shown in Figure 7b. This approach is highly versatile, enabling the production of dense components from metals, composites, ceramics, and polymers with intricate geometries and dimensions ranging from a few millimeters to several hundred millimeters in size.[100−102] The process can be further classified as selective laser sintering (SLS), selective laser melting (SLM), and electron beam melting (EBM). When the energy beam interacts with the material, a molten pool is formed. This molten pool solidifies and results in a unique microstructure characterized by grain orientation along the thermal gradient, contributing to anisotropic behavior.[103]

The PBF process is governed by a complex interaction of physical mechanisms, including conductive, radiative, and convective heat transfer as well as mass transport driven by surface tension and thermally driven capillary flow.[104] Dimensionless parameters of fluid flow and thermal analysis[105] are required for explaining the physics of the process. A key process metric for predicting the resultant microstructure is the volumetric energy density (E_V), defined as

$$E_V = \frac{P}{vhd} \tag{5}$$

where P, v, h, and d represent the beam power, scan speed, hatch spacing, and layer thickness, respectively.

Shi et al.[106] investigated the p-type $Bi_{0.5}Sb_{1.5}Te_3$ material synthesized using LPBF techniques. The laser process parameters used in this work were (P = 60 W, v = 250−400 mm/s, spot size = 100 μm, and scanning distance = 50 μm). The increase in E_V from 1.5 to 2.3 J/mm^3 reduces the nanoporosity ratio from 1/150 to 1/400. However, for an E_V of 2.4 J/mm^3, the ratio of nanopores increased to 1/70 due to evaporation of the elements at high energy. Hence, an optimized energy is required for synthesizing the material. The thermoelectric properties exhibited significant anisotropy, with the electrical conductivity along the building direction being twice that of the perpendicular direction (~35 S/cm). The peak zT reached 1.1 at 348 K along the building direction, attributed to low thermal conductivity (0.9 W/m K). The relationship between power factor and E_V was modeled by a second-order polynomial, offering a predictive framework for optimizing thermoelectric performance. Baudry et al.[103] investigated the AM of SiGe thermoelectric materials using LPBF. A laser power of 99 W with a scanning speed of 400 mm/s and a spot size of 70 μm was used. The relative density of these samples ranges from 91.8 to 96.6%. Composition analysis showed a slight reduction in phosphorus content due to vaporization. Microstructural analysis using SEM and electron backscatter diffraction (EBSD) highlighted the presence of columnar structures and substructures within grains, along with cracks and defects aligned with the laser tracks. These cracks result in a decrease in electrical conductivity (~40 S/cm) compared to the sample synthesized with spark plasma sintering (~80 S/cm). Overall, the obtained zT (0.11 at 873 K) was lower than the reference values for SiGe, indicating further LPBF process optimization is required. Oztan et al.[107] studied Bi_2Te_3 using 20−35 W laser power, 250−400 mm/s scan speed, and 50 μm spot size. The smooth melt tracks were seen at 25−30 W and 300−350 mm/s, while 35 W caused balling, and low power gave irregular tracks. The best condition (25 W, 350 mm/s, 5 scans) reduced defects, but EDS analysis at 10 points showed 2−450% composition variation, indicating strong inhomogeneity.

Welch et al.[108] examined the LPBF processing of SiGe alloys. Laser power ranging from 25 to 75 W is used for fabricating $Si_{50}Ge_{50}$ and $Si_{80}Ge_{20}$ samples, with a hatch distance of 37.5 to 50 μm, a scan speed of 25 to 600 mm/s, and a spot size of 50 μm. The XRD data reveal the presence of the SiO_2 phase after laser powder bed fusion. The EBSD pattern showed that the grain diameter median is ~25 μm for the $Si_{50}Ge_{50}$ sample. The fabricated $Si_{50}Ge_{50}$ and $Si_{80}Ge_{20}$ materials exhibit high porosity (56−64%), oxide formation, and Ge-rich segregation. This results in electrical conductivity below ~10 S/cm and a zT of only ~0.06 at 673 K for $Si_{80}Ge_{20}$. However, the study is strengthened by detailed EBSD and thermoelectric characterization. The main challenges are high porosity, residual SiO_2, and unquantified impurities, which make the interpretation of the p-type behavior uncertain. This suggests that improved atmosphere control, densification, and chemical analysis are essential for additively manufactured SiGe.

Two primary techniques for LPBF are the SLS and SLM. SLS uses a high-power laser to sinter-powdered industrial materials at an atomic level, forming solid parts layer by layer. This technique exhibits remarkable adaptability and can handle a wide variety of materials, making it suitable for fabricating thermoelectric materials with intricate geometries and an improved robustness. Conversely, SLM involves heating powdered materials until they fully melt and fuse together, which is especially effective for achieving dense and strong final components. These techniques are discussed in the following section.

2.2.1.1. Selective Laser Sintering (SLS). Shi et al.[56] investigated the fabrication of porous $Bi_{0.5}Sb_{1.5}Te_3$ thermoelectric materials using SLS. A 30 W laser with a scan speed of 3200 mm/s and a scan spacing of 50−80 μm (spot size ≈300 μm) was used to fabricate the sample. In the XRD data, the formation of an oxide phase is observed. However, the report identifies this impurity peak as less significant, although the peak intensity of the impurity phase is higher than the BST phase peak. The study reports that the porous $Bi_{0.5}Sb_{1.5}Te_3$ samples exhibit an electrical conductivity of 4.03×10^2 S/cm and a reduced thermal conductivity of 0.27 W/m K, resulting in a zT of 1.29 at 327 K. The research underscores the efficiency and geometric flexibility of SLS 3D printing, which minimizes material waste and enables the production of complex shapes. Further work is needed to improve mechanical strength and extend the technique to other thermoelectric materials.

2.2.1.2. Selective Laser Melting (SLM). Zhang et al.[57] examined a manufacturing approach for Bi_2Te_3 powder using SLM. The powder was spread inside a thin stainless-steel ring and processed each layer with a 1070 nm diode-pumped Ytterbium fiber laser in a nitrogen environment. The SLM process built eight layers, each approximately 150 μm thick. The increase in laser power from 16 to 25 W results in an increase in the density value from 81 to 88%. The other parameters are kept constant (laser spot size 50 μm, scan speed 500 mm/s, and hatch distance 37.5 μm). SEM imaging showed that the surface pore sizes are approximately 5 μm or larger, and with good fusion between layers. Additionally, in the XRD analysis, the Bi_2Te_3 phases were indexed. The reported zT value was 0.11 at 323 K. Qiu et al.[109] investigated a method combining thermal explosion with SLM to fabricate p-type $Bi_{0.4}Sb_{1.6}Te_3$ materials that exhibit high thermoelectric performance and mechanical robustness. The observed compressive strength for this material is 91 MPa, higher than that of spark plasma sintered (SPS) samples (80 MPa). The resulting material exhibits an oriented grain structure with an orientation factor of up to 0.9 and a peak zT of 1.1 at 316 K. This advancement enables the fabrication of TE legs to small sizes and the assembly of effective micro-TE modules, providing a practical solution for creating robust, high-performance thermoelectric devices.

Wu et al.[110] explored a cost-effective fabrication method that combines noncontact dispenser printing with SLM to produce n-type Bi_2Te_3-based materials. The $Bi_2Te_{2.7}Se_{0.3}$ sample is synthesized using self-propagating high-temperature synthesis (SHS). For preparing a slurry, $Bi_2Te_{2.7}Se_{0.3}$ was stirred with Tween 20 (CAS: 9005-64-5) and antifoam AR (CAS: P11172) and ball-milled for 18 h. This results in the removal of the bubble, making the slurry more viscous. After the slurry was made, the next step was to use the dispenser printing, followed by SLM. For the SLM process, a laser power of 6 W, a scanning rate of 80 mm/s, and an E_V of 16.67 J/mm^3 were used. SEM imaging reveals that no balling effect is observed after the SLM process. However, for a low-energy density of 10 J/mm^3, surface balling is visible in the SEM imaging. A power factor of 1.5 mW/m K^2 is observed, which is lower than that of the sample synthesized from SHS (2.5 mW/m K^2) at 300 K. This fabrication method exhibits greater efficiency in material usage and manufacturing time. This approach enhances powder quality and additive selection, enabling scalable, low-cost production of TE modules and supporting the wider adoption of eco-friendly thermoelectric technologies.

Yan et al.[111] explored a methodology that combines SHS with SLM. The research emphasizes the fabrication of the ZrNiSn material on a titanium (Ti) substrate. In this report, laser power (P) ranges from 12 to 28 W, with varying scan speeds (v) from 40 to 200 mm/s and a laser spot size of 100 μm. The four regions were categorized based on the energy density: overheated region ($E_V \geq 220$ J/mm^3), distorted region ($146 < E_V < 220$ J/mm^3), flat area ($88 < E_V < 146$ J/mm^3), and balling region ($E_V < 88$ J/mm^3). In the overheated region, the energy is much higher, which partially melted the unscanned powder. Also, for this energy, some elements evaporated (Sb or Sn). For the distortion area, a fluctuation in layer thickness was observed. For the flat region, on the surface, no ridge-like features were formed. For the low-energy density, the energy was insufficient to melt the powder completely, and a balling effect was observed. The identified optimal parameters for SLM processing were $P = 18$ W, $\nu = 80$ mm/s, and hatch spacing = 30 μm. The ZrNiSn processed via SLM exhibited a peak zT = 0.39 at 873 K. Moreover, the interface between the ZrNiSn layer and the Ti substrate demonstrated robust adhesion and minimal contact resistance. The findings suggest that the SHS-SLM technique is a promising strategy for the rapid fabrication of TE materials and devices.

Zhou et al.[112] investigated the SLM for producing TEGs, aiming to improve the efficiency and cost-effectiveness. Success with SLM hinges on optimizing powder characteristics such as particle size, shape, and flowability. Experimental analyses indicate that improvements in powder properties are essential for effective SLM processing. A model was developed by Zhou et al. to predict the requirement for preparing high-density samples using the SLM technique. The model calculates the relationship between energy absorption (Q_a) and energy consumption (Q_c) based on the surface structure of metallic powder, the porosity of the powder bed, heat loss, and vaporization. The energy equation for SLM can be written as follows:

$$Q_a \geq Q_{\text{melting}} + Q_{\text{vaporization}} + Q_{\text{heat loss}} \quad (6)$$

where Q_{melting} refers to the energy consumed in melting the powder, $Q_{\text{vaporization}}$ is the energy consumed during powder vaporization, and $Q_{\text{heat loss}}$ represents the energy loss due to heat convection, conduction, and radiation. For the surface structure of the powder, an X-ray photoelectron spectroscopy (XPS) depth profiling experiment was performed. This developed model predicted that the Q_a by the local powder bed is 3 to 8 times higher than the Q_c for making the dense sample (relative density 97−99%). This model was verified by synthesizing the high-entropy alloy CrMnFeCoNi using SLM. This model also suggested that the presence of oxide layers on powder surfaces and the porosity within the powder bed enhance the laser absorptivity. This enhancement is particularly useful for materials with inherently low absorptivity, such as copper and copper-based alloys.

Shi et al.[113] fabricated Sb_2Te_3 using SLM with laser power of 60−100 W, scan speed of 200−300 mm/s, and spot size of 80 μm. Best results (60 W, 300 mm/s) showed near-nominal composition, but density was low (91%) and other settings caused composition deviation. Laser energy density affects the structure and improves the power factor up to 1.9 mW/(m K^2) at 320 K. SLM allows control of properties, giving uniform materials with performance similar to traditional methods and enabling complex shapes.

Desouky et al.[114] studied how energy density affects the microstructure and consolidation of selective laser-melted Bi_2Te_3 powder using a ProXTM 100 SLM system (50 W, 1070 nm), with laser power 10−25 W, 100 μm spot size, and 350 mm/s scan speed. They found that higher laser power improves consolidation and reduces porosity, with the lowest porosity at 25 W, showing that optimizing SLM parameters can enhance structural properties for additive manufacturing.

Wu et al.[115] developed a three-dimensional physical model for SLM of Mg_2Si powder containing 10% Si nanoparticles, incorporating the conservation of mass, momentum, energy, and nanoparticle transport. However, its predictive strength is constrained by several simplifying assumptions. The model uses constant material properties, which include a specific heat of 67.87 J/(kg-K), thermal conductivity of 7.0 W/(m K) in the solid state and 5.0 W/(m K) in the liquid state, a density of 1.99 g/cm^3, and a latent heat of 4.5×10^5 J/kg. However, it does not consider the effect of nanoparticle size, which becomes important at the nanoscale. The simulations report shrinkage depths reaching approximately 0.06 mm at 18.75 W and 20 mm/s, along with peak surface temperatures varying from 1175 K (at 6.25 W) to 2075 K (at 25 W). These results emphasize the narrow processing window bounded by the melting temperatures of Mg_2Si (1375 K) and Si (1687 K). Melt pool velocities on the order of 10^{-4} mm/s, combined with the observed flow patterns, lead to nanoparticle migration toward the boundaries, which can diminish compositional uniformity. The model suggested an optimal parameter set of 18.75 W, a scanning speed of 100 mm/s, and a laser diameter of 0.3 μm to minimize shrinkage and particle aggregation. However, its dependence on single-phase assumptions and the absence of direct experimental validation for Mg_2Si limit overall confidence in the predictions.

Desouky et al.[116] reported that selective laser melting (SLM) enabled the direct consolidation of thermoelectric legs onto substrates. Preliminary trials with Bi_2Te_3 powders demonstrated that SLM can achieve melt depths (>50 μm) greater than the largest particle size (45 μm). The powders were cold-pressed into discs with a diameter of 6 mm and a thickness of 0.5 mm at 295 MPa prior to laser irradiation using a 527 nm Nd:YLF laser operating at 5 kHz with 500 ns pulses. For energy densities of the laser beam of 0.8×10^{-2} J/mm^2 (3 W) and 1.2×10^{-2} J/mm^2 (5 W), a Gaussian beam profile caused a nonuniform energy distribution. The maximum intensity at the 300 μm beam center produced fully fused tracks approximately 290 μm wide at 3 W and 420 μm wide at 5 W. In contrast, partial fusion along the edges resulted in shallow melt depths of <10 μm at 3 W and 50 μm at 5 W due to reduced intensity. A steep thermal gradient, resulting from rapid heating and cooling, generated random microcracks along the melt tracks due to the Gaussian energy distribution. These findings highlight the need for process optimization, such as beam shaping to flatten the profile, adjusting the energy distribution, or refining scan strategies to achieve uniform densification and minimize cracking.

According to Zhan,[66] a combination of SHS and SLM is employed to produce dense n-type BiTeSe materials from elemental Bi, Te, and Se powders on a large scale. During laser processing, reactions among Bi, Te, and Se occur within the molten pool, forming a highly oriented, dense microstructure that enhances carrier mobility. A sample with dimensions of 60 × 30 × 0.5 mm^3 is printed in under an hour. In thermoelectric power generation mode, the open-circuit voltage reaches 324 mV, with a peak power output of 4.97 mW under a temperature difference of 40 K.

SLS/SLM techniques enable the fabrication of complex geometries and are well-established for metals such as stainless steel, aluminum, titanium, cobalt−chromium, silver, and copper. Their disadvantages include high laser costs and the evaporation of volatile TE elements under intense heat, which causes stoichiometric deviation. TE materials also possess lower melting points and thermal shock resistance, making SLS/SLM processing challenging.

Table 3 summarizes the AM techniques used to fabricate various thermoelectric materials. It further highlights the principles, resolutions, advantages, disadvantages, and scalability of different AM techniques.

3. ADDITIVE MANUFACTURING WITH MACHINE LEARNING

Recent studies have used AI and machine learning methods to predict thermoelectric properties, improve device performance, and assist in the fabrication process. Common supervised models include artificial and deep neural networks (ANN/DNNs), random forests (RFs), gradient boosting methods like XGBoost, and Gaussian process regression (GPR). For design optimization, researchers commonly use genetic algorithms (GAs) along with other evolutionary techniques. For example, Zhu et al. trained a deep ANN with 5 layers of 400 neurons using 5000 FEM simulation data points.[121] This model predicted thermoelectric generator performance, such as power density and efficiency, with more than 98% accuracy. They then combined the model with a genetic algorithm to optimize the leg geometry in about 40 s, which is more than 1000 times faster compared to using FEM alone.[121] Tree-based models have also shown strong results. For $Bi_2Te_{3-x}Se_x$ thermoelectric materials, Vipin et al. reported that a random forest model achieved R^2 values of about 0.90−0.95 for predicting electrical conductivity, thermal conductivity, Seebeck coefficient, and zT.[122] These results show that the method can accurately predict material properties even when only limited data is available.

In recent years, the integration of data-driven methodologies with AM has attracted considerable attention for accelerating materials design and process optimization. Machine learning (ML), a subset of artificial intelligence (AI), enables the prediction of outcomes from training data sets without the need for explicit programming. In the field of thermoelectric materials, several recent studies have demonstrated the combined use of ML and AM to enhance material performance and improve process efficiency. In a notable study, Florenciano et al. developed flexible thermoelectric generators (TEGs) aimed at powering wearable and IoT applications using laser-based additive manufacturing techniques.[123] Specifically,

Table 3. Summarizes the Material Used, Principle, Resolution, Advantages, Disadvantages, and Scalability for Different AM Methods

method	materials	principle	resolution	advantage	disadvantage	scalability
FDM (material extrusion)	thermoplastics: • polylactic acid (PLA) • acrylonitrile butadiene styrene (ABS) thermoelectric fillers: • $Bi_{0.5}Sb_{1.5}Te_3$ (BST) • Bi_2Te_3 additives: • multiwalled carbon nanotubes • ZnO composites: • PLA/BST composites • ABS/Bi_2Te_3 composites • CABS/ZnO	thermoplastic filament extrusion through a heated nozzle	~50−200 μm[117]	low cost, simple, widely available, multimaterial printing capability	low electrical conductivity, oxidation risk, poor surface finish	high
DIW (material extrusion)	TE powders: • $(Bi,Sb)_2(Te,Se)_3$ • Bi_2Te_3 • $Bi_{0.5}Sb_{1.5}Te_3$ • $Nb_{1-x}CoSb$ • Half-Heusler $Ti_{1.75}Zr_{0.25}Ni_{1.5}Fe_{0.5}SnSb$ Nanostructures: • Bi_2Te_3 nanowires binders/polymers: • polyvinylpyrrolidone solvents/ink systems: • ethanol−ethylene glycol mixture • glycerol dopants: • Na-doping ($Bi_2Te_{2.7}Se_{0.3}$ system) chalcogenidometallates (for viscoelastic inks)	extrusion of viscoelastic ink/slurry	>100 μm (typical, lower than SLA)[117]	multimaterial, complex shapes, scalable.	porosity, shrinkage, and dimensional inaccuracy	high
SLA (vat photopolymerization)	photopolymer resins TE fillers: • $Bi_{0.5}Sb_{1.5}Te_3$ composite systems: • resin + TE powders (40−60 wt %)	UV laser curing of resin	~10 μm[117]	excellent surface finish, high resolution, smooth surface finish	high porosity, limited materials, support required	moderate
DLP (vat photopolymerization)	materials used: • UV-sensitive resins: • diurethane dimethacrylate • isobornyl acrylate • thermoelectric fillers: • Ag_2Se • Bi_2Te_3 • Sb_2Te_3 • conductive additives:	projected UV curing	~10−50 μm (high resolution)[118]	fast printing, good mechanical properties	limited TE performance, resin complexity	moderate

Table 3. continued

method	materials	principle	resolution	advantage	disadvantage	scalability
	• PEDOT: PSS-coated Ag_2Se nanowires • structures: • polymeric microlattices (later coated with TE materials)					
material jetting	liquid inks: • thermoelectric nanoparticle suspensions TE materials: • Bi_2Te_3-based inks polymers/binders: • Inkjet-compatible polymer matrices	droplet deposition and UV curing	25−50 μm[119]	high accuracy, smooth surface, multimaterial	low zT, material degradation	moderate
PBF (SLS/SLM)	thermoelectric powders: • Bi_2Te_3 • Sb_2Te_3 other alloys: • metal powders suitable for laser sintering/melting chalcogenides	laser/e-beam melting of powders	~20−80 μm (laser spot size dependent)[120]	dense parts, complex geometry, high performance	high cost, element evaporation, and anisotropy	moderate−High

$Bi_{0.5}Sb_{1.5}Te_3$-based materials were fabricated on flexible substrates through advanced laser printing approaches. A key innovation in this work was the integration of ML to guide and optimize the fabrication process. By training models on experimental data sets, the study systematically identified critical parameters such as Sb concentration, printing atmosphere, and laser energy that strongly influence the thermoelectric power factor. This data-driven approach enabled efficient exploration of the complex processing−composition space, which would otherwise require extensive trial-and-error experimentation. The ML-optimized conditions resulted in a measurable enhancement in performance, with approximately a 4% increase in the power factor, reaching values around 1280 $\mu W/m\ K^2$. Furthermore, the fabricated flexible TE module, with an area of 4 cm^2, demonstrated a power output of 44 μW at a temperature difference (ΔT) of 30 K.[123]

Song et al. developed a Gaussian process regression (GPR)-based ML model for predicting the optimized ink formulation and printing parameter for a high-power factor.[124] This approach facilitated the identification of optimal printing conditions, resulting in a high figure of merit (zT) of 1.3 at room temperature for BiSbTe-based materials.[124] Zhang et al. fabricated three-dimensional Bi_2Te_3 structures using laser powder bed fusion (LPBF).[57] However, the printed components exhibited a relatively low density (∼88%), underscoring the challenge of achieving adequate densification through conventional tuning of AM process parameters. To address these limitations, Headley et al. implemented an iterative ML-assisted AM framework to predict laser−material interactions and melt pool geometries for Bi_2Te_3 systems.[125] Under optimized processing conditions (laser power = 25 W, hatch spacing = 80 μm, scan speed = 400 mm/s, and layer thickness = 75 μm), a crack-free and highly dense (>99%) n-type $Bi_2Te_{2.7}Se_{0.3}$ sample was successfully fabricated using LPBF. Furthermore, complex geometries, including hollow rectangular structures, rectangular prisms, and trapezoidal configurations of $Bi_2Se_{2.7}Te_{0.3}$, were also realized. These findings demonstrate that the integration of ML with AM not only accelerates the identification of optimal processing parameters but also enables the fabrication of high-density materials with enhanced properties.

This study clearly illustrates the emerging paradigm of "materials-by-design," where ML accelerates discovery by pinpointing optimal processing and material configurations within vast parameter spaces. Such integration not only improves device performance but also significantly reduces development time and experimental costs, marking a crucial step toward scalable and high-efficiency thermoelectric technologies.

4. CHALLENGES AND FUTURE DIRECTIONS

The fabrication of thermoelectric materials with polymer matrixes or other binding agents can alter their intrinsic properties. AM processes, such as DIW, FDM, and PBF, require precise control over parameters such as temperature, speed, and layer thickness. Optimizing these parameters is crucial for achieving the optimal performance of the thermoelectric material, a process that can be time-consuming. One solution to reduce the time and optimize parameters is to incorporate an ML-assisted data-driven approach. Additionally, to achieve high performance, functional-graded thermoelectric materials are required, which have a high average zT. Below are some challenges and their future direction:

One major challenge is material compatibility and long-term stability. Many highly efficient thermoelectric materials (Bi_2Te_3, Sb_2Te_3) have low melting temperatures and easily oxidize when exposed to air during the printing or heat-treatment stages. Since most AM methods depend on binders or solvents, choosing an unsuitable formulation can result in unwanted porosity and reduced device performance. SLA/DLP-printed composites containing 40−60 wt % $Bi_{0.5}Sb_{1.5}Te_3$ became highly porous after binder burnout, resulting in low thermal conductivity (~0.2 W/m K) but a limited zT of ~0.12.[54] Geometric precision and microstructural control also pose ongoing difficulties. Additive manufacturing can introduce shrinkage, voids, and anisotropic microstructures, influencing electrical transport and overall durability. A notable example is DIW-printed Cu_2Se honeycomb structures, which experienced 60−70% linear shrinkage during sintering. Although the external shape was preserved, the high shrinkage risked deformation, cracking, and internal stress accumulation.[46]

Developing hybrid manufacturing strategies will help to overcome the limitations of single-method systems. Combining processes such as DIW with selective laser melting could enable better densification, electrical pathways, and structural integrity. AI-assisted optimization may further refine the design and process conditions, helping to create highly efficient and customized TE devices.

Current AM-based functionally graded thermoelectric materials are fabricated by sequential deposition of BiSbTe compositions. These segmented legs operate up to a temperature gradient of ~240 K. The measured electrical resistance shows a slight increase (32 mΩ) compared to the simulated value (20 mΩ), which is attributed to the interface formed between the sequentially printed segments. These samples were annealed for 6 h at 523 K, and the output performance remained unchanged.[51] However, this single thermal treatment is not enough to assess long-term stability.

In comparison, conventionally synthesized segmented modules based on two different thermoelectric material classes (GeTe and Bi_2Te_3) can operate over a high-temperature gradient (ΔT = 449 K) with an efficiency of 15.5%.[51] To achieve similar high-ΔT performance using AM, the choice of the material is essential. These materials must exhibit similar compatibility factors and coefficients of thermal expansion over the operational temperature range. Additionally, heat-cycle measurements are necessary to investigate potential changes in composition, interlayer diffusion at elevated temperatures, grain growth, and mechanical durability during operation.

The electrical and thermal conductivity of additively manufactured thermoelectric materials is affected by porosity and grain size. High porosity reduces electrical conductivity and affects thermal transport and mechanical stability. Therefore, achieving high relative density (~95% or higher) is essential for optimal device performance. To achieve this density for the AM-based fabricated material, the synthesis parameters need to be optimized. This makes the AM technique time-consuming. By utilizing the ML approach, high-density samples with fewer trials are possible. Hence, for future directions, the AM technique can be combined with ML, which predicts optimized parameters and fabricates high-density thermoelectric materials. Additionally, postprocessing steps such as sintering are critical in reducing porosity and improving interparticle connectivity.

Beyond material-level considerations, electrical contacts and device packaging present additional challenges. The formation of low-resistance and thermally stable electrical contacts between thermoelectric legs and electrodes is crucial to efficient device performance. However, surface roughness, residual porosity, and compositional inhomogeneity in AM-fabricated materials can increase the contact resistance and degrade performance. Furthermore, reliable packaging is essential to protecting devices from oxidation, mechanical degradation, and thermal cycling during operation. Unlike conventional thermoelectric modules, where packaging strategies are well-established, AM-based devices still require the development of robust encapsulation and interface engineering approaches to ensure long-term stability.

Currently, most researchers utilizing additive manufacturing are focused on fabricating thermoelectric materials rather than complete devices. Future progress will depend on improving multimaterial printing so that both p-type and n-type legs can be fabricated together in a single process while also developing binder-free or low-binder inks to enhance charge transport. There is also a need for in situ densification methods to reduce porosity during printing itself, along with the use of machine learning-based optimization to better control process parameters and improve performance. In addition, establishing clear standards will be important to support reliable and scalable industrial adoption.

5. CONCLUSIONS

This review explores the potential of AM in the domain of TE materials and devices, emphasizing advancements, methodologies, and applications. Traditional thermoelectric fabrication methods often face challenges including high material wastage and limited geometrical flexibility. In contrast, AM technologies enable the layer-by-layer creation of intricate structures, minimizing the material wastage. The FGM leg fabricated using DIW exhibited a 20% improvement in power density compared with the homogeneous leg.[58] Various infill techniques and leg geometries have been investigated, such as a honeycomb structure, which demonstrated a 25.6% improvement in efficiency compared with the solid design.[88] Additionally, the hourglass-shaped leg exhibited 3.6 times greater efficiency than the conventional cuboid design.[87] Recent studies have predominantly focused on DIW due to notable advancements in printer technology and enhancements in thermoelectric printing inks. Notably, the highest reported efficiency of 8.7% was achieved by using DIW to fabricate segmented BST structures with compositionally graded layers.[51] The ability to fabricate flexible and wearable TEGs using advanced inks and composites has expanded the energy-harvesting solutions for wearable electronics and IoT applications. However, despite the benefits of AM, it still faces certain limitations related to productivity, postprocessing, and trade-offs concerning material properties. Currently, it seems like DIW could be better suited to the production of TE devices due to its capability to print multimaterial parts and complex structures, whereas FDM and material jetting are applicable in cheap prototyping and flexible electronics. On the other hand, the laser-based processes of SLS and SLM could ensure a higher density and performance. They face challenges such as high costs, high-energy consumption, and potential loss of volatile elements, making them unsuitable for mass production. Despite being inferior to bulk TEs in intrinsic performance, TE devices produced using AM technologies have an edge in terms of being predominantly focused.

Even though there has been significant progress, thermoelectric devices made using additive manufacturing (AM) still do not perform as well as bulk materials. This is mainly due to several challenges, such as high porosity and low density, which reduce electrical conductivity and the use of binders, which can hinder smooth charge carrier transport. In addition, printed devices often suffer from interfacial and contact resistance, further affecting the performance. High-temperature processes such as selective laser melting can also lead to material degradation or evaporation. Another limitation is the difficulty in integrating multiple materials, which restricts the fabrication of the complete devices. Because of all of these factors, AM-based thermoelectric devices are still unable to reach the performance levels of conventionally sintered materials. Techniques such as DIW and inkjet printing are relatively low cost and scalable but suffer from performance limitations because of binder use. In contrast, powder bed fusion methods can produce dense structures but are expensive and difficult to scale because of high-energy requirements and material losses. Furthermore, maintaining the composition control and uniformity during large-scale production remains challenging. Therefore, future work should focus on hybrid manufacturing approaches and process optimization for an industrial-scale deployment.

Figure 2c shows that additive manufacturing of thermoelectric materials clearly depends on the process used. Only a few cases reach high performance, with maximum zT values around 1.3−1.4, such as DIW (PbTe/Na ∼1.4) and SLS ($Bi_{0.5}Sb_{1.5}Te_3$ ∼1.3). Most other methods fall in the range of 0.4−1.1, showing a noticeable gap compared to bulk materials, which can reach zT values of about 1−2 or higher. DIW and SLS perform better mainly because they allow higher material loading and better densification. In contrast, DLP and SLA show moderate results, while FDM is limited due to the use of polymers. Overall, performance is still restricted by issues like porosity, binder content, composition instability, and resistance between printed layers.

The study concludes that the development of AM and TE technologies can lead to more efficient, customizable, and sustainable energy systems, making significant contributions to the fields of energy harvesting

AUTHOR INFORMATION

Corresponding Author

Ramesh Chandra Mallik − *Thermoelectric Materials and Devices Laboratory, Department of Physics, Indian Institute of Science, Bangalore 560012, India;* orcid.org/0000-0002-8383-7812; Email: rcmallik@iisc.ac.in

Authors

R S Kondaguli − *B.L.D.E A's V.P Dr. P G Halakatti College of Engg & Technology, (Affiliated to Visvesvaraya Technological University), Vijayapur, Karnataka 586103, India*

Inder Kumar − *Thermoelectric Materials and Devices Laboratory, Department of Physics, Indian Institute of Science, Bangalore 560012, India*

C R Hiremath − *B.L.D.E A's V.P Dr. P G Halakatti College of Engg & Technology, (Affiliated to Visvesvaraya Technological University), Vijayapur, Karnataka 586103, India*

P V Malaji − *B.L.D.E A's V.P Dr. P G Halakatti College of Engg & Technology, (Affiliated to Visvesvaraya Technological University), Vijayapur, Karnataka 586103, India*

Somashekara Makireddypalli Adinarayanappa − *Additive Manufacturing and 4D Printing Laboratory, Department of Mechanical, Materials and Aerospace Engineering, Indian Institute of Technology Dharwad (IIT Dh) Dharwad, Dharwad 580011, India*

Complete contact information is available at:
https://pubs.acs.org/10.1021/acsami.6c04499

Author Contributions

[†]R.S.K. and I.K. made equal contributions to this manuscript.

Notes

The authors declare no competing financial interest.

ACKNOWLEDGMENTS

The author, R.S.K., would like to acknowledge the Indian Academy of Sciences (PHYT5) for their support. I.K. thanks the Council of Scientific & Industrial Research funding agency for the CSIR-SPM fellowship [Award No SPM/09/0079(13446)/2022-EMR-I].

REFERENCES

(1) Sarkar, A.; Somashekara, M. A.; Paranthaman, M. P.; Kramer, M.; Haase, C.; Nlebedim, I. C. Functionalizing Magnet Additive Manufacturing with In-Situ Magnetic Field Source. *Addit. Manuf.* **2020**, *34*, No. 101289.

(2) Shaukat, H.; Ali, A.; Ali, S.; Altabey, W. A.; Noori, M.; Kouritem, S. A. Applications of Sustainable Hybrid Energy Harvesting: A Review. *Journal of Low Power Electronics and Applications* **2023**, *13* (4), 62.

(3) Qasem, N. A. A.; Abdulrahman, G. A. Q.; Osinkin, D. A Recent Comprehensive Review of Fuel Cells: History, Types, and Applications. *Int. J. Energy Res.* **2024**, *2024* (1), 7271748.

(4) Hao, D.; Qi, L.; Tairab, A. M.; Ahmed, A.; Azam, A.; Luo, D.; Pan, Y.; Zhang, Z.; Yan, J. Solar Energy Harvesting Technologies for PV Self-Powered Applications: A Comprehensive Review. *Renew. Energy* **2022**, *188*, 678−697.

(5) López, E.; Artacho, I.; Datas, A. Thermophotovoltaic Conversion Efficiency Measurement at High View Factors. *Sol. Energy Mater. Sol. Cells* **2023**, *250*, No. 112069.

(6) Habibi, M.; Yelishala, S. C.; Zhu, Y.; Tervo, E. J.; Steiner, M. A.; Cui, L. Enhanced Power Density in Zero-Vacuum-Gap Thermophotovoltaic Devices. *Energy Environ. Sci.* **2025**, *18* (3), 1514−1523.

(7) Shah, R. N. A. R. A.; Redzuan, F. L. M.; Zaki, S. A.; Mohammad, A. F.; Yakub, F. A Review on Thermoelectric Generators: Structural Optimization and Economic Analysis. *J. Adv. Res. Fluid Mech. Therm. Sci.* **2023**, *105* (2), 99−114.

(8) Ge, M.; Li, Z.; Zhao, Y.; Xuan, Z.; Li, Y.; Zhao, Y. Experimental Study of Thermoelectric Generator with Different Numbers of Modules for Waste Heat Recovery. *Appl. Energy* **2022**, *322*, No. 119523.

(9) Kucova, T.; Prauzek, M.; Konecny, J.; Andriukaitis, D.; Zilys, M.; Martinek, R. Thermoelectric Energy Harvesting for Internet of Things Devices Using Machine Learning: A Review. *CAAI Trans. Intell. Technol.* **2023**, *8* (3), 680−700.

(10) Luo, H.; Yang, T.; Jing, X.; Cui, Y.; Qin, W. Environmental Energy Harvesting Boosts Self-Powered Sensing. *Mater. Today Energy* **2024**, *40*, No. 101502.

(11) Yang, S.; Li, Y.; Deng, L.; Tian, S.; Yao, Y.; Yang, F.; Feng, C.; Dai, J.; Wang, P.; Gao, M. Flexible Thermoelectric Generator and Energy Management Electronics Powered by Body Heat. *Microsyst. Nanoeng.* **2023**, *9* (1), 106.

(12) Li, A.; Wang, L.; Li, J.; Wu, X.; Mori, T. Self-Optimized Contact in Air-Robust Thermoelectric Junction towards Long-Lasting Heat Harvesting. *Nat. Commun.* **2025**, *16* (1), 1502.

(13) Fu, Y.; Ai, X.; Hu, Z.; Zhao, S.; Lu, X.; Huang, J.; Huang, A.; Wang, L.; Zhang, Q.; Jiang, W. Interface Kinetic Manipulation Enabling Efficient and Reliable Mg3Sb2 Thermoelectrics. *Nat. Commun.* **2024**, *15* (1), 9355.

(14) Liu, Y.; Wang, X.; Hou, S.; Wu, Z.; Wang, J.; Mao, J.; Zhang, Q.; Liu, Z.; Cao, F. Scalable-Produced 3D Elastic Thermoelectric Network for Body Heat Harvesting. *Nat. Commun.* **2023**, *14* (1), 3058.

(15) Tang, X.; Li, Z.; Liu, W.; Zhang, Q.; Uher, C. A Comprehensive Review on Bi2Te3-Based Thin Films: Thermoelectrics and Beyond. *Interdisciplinary Materials* **2022**, *1* (1), 88−115.

(16) Lin, H.; Yang, M.; Ru, X.; Wang, G.; Yin, S.; Peng, F.; Hong, C.; Qu, M.; Lu, J.; Fang, L.; Han, C.; Procel, P.; Isabella, O.; Gao, P.; Li, Z.; Xu, X. Silicon Heterojunction Solar Cells with up to 26.81% Efficiency Achieved by Electrically Optimized Nanocrystalline-Silicon Hole Contact Layers. *Nat. Energy* **2023**, *8* (8), 789−799.

(17) Gu, H.; Fei, C.; Yang, G.; Chen, B.; Uddin, M. A.; Zhang, H.; Ni, Z.; Jiao, H.; Xu, W.; Yan, Z.; Huang, J. Design Optimization of Bifacial Perovskite Minimodules for Improved Efficiency and Stability. *Nat. Energy* **2023**, *8* (7), 675−684.

(18) Goldsmid, H. J.*Introduction to Thermoelectricity*; Springer Series in Material Science: New York, 2010.

(19) Zhu, H.; Deng, Z.; Qu, Y.; He, P.; Geng, H. Cu-In Co-Doping and Layered Directional Sintering for High Thermoelectric Efficiency and Mechanical Strength in Bi2(Te,Se)3. *Adv. Funct. Mater.* **2025**, *35* (19), 2422007.

(20) Yin, L.; Liu, W.; Li, M.; Wang, D.; Wu, H.; Wang, Y.; Zhang, L.; Shi, X.; Liu, Q.; Chen, Z. Interstitial Cu: An Effective Strategy for High Carrier Mobility and High Thermoelectric Performance in GeTe. *Adv. Funct. Mater.* **2023**, *33* (25), 2301750.

(21) Zhou, C.; Lee, Y. K.; Yu, Y.; Byun, S.; Luo, Z. Z.; Lee, H.; Ge, B.; Lee, Y. L.; Chen, X.; Lee, J. Y.; Cojocaru-Mirédin, O.; Chang, H.; Im, J.; Cho, S. P.; Wuttig, M.; Dravid, V. P.; Kanatzidis, M. G.; Chung, I. Polycrystalline SnSe with a Thermoelectric Figure of Merit Greater than the Single Crystal. *Nat. Mater.* **2021**, *20* (10), 1378−1384.

(22) Chen, J.; Dong, Z.; Li, Q.; Ge, B.; Zhang, J.; Zhang, Y.; Luo, J. Enhanced Thermoelectric Performance in Vacancy-Filling Heuslers Due to Kondo-Like Effect. *Adv. Mater.* **2024**, *36* (33), 2405858.

(23) Jaziri, N.; Boughamoura, A.; Müller, J.; Mezghani, B.; Tounsi, F.; Ismail, M. A Comprehensive Review of Thermoelectric Generators: Technologies and Common Applications. *Energy Rep.* **2020**, *6*, 264.

(24) Oztan, C.; Welch, R.; Leblanc, S. Additive Manufacturing of Bulk Thermoelectric Architectures: A Review. *Energies* **2022**, *1*, 3121.

(25) Zhou, L.; Miller, J.; Vezza, J.; Mayster, M.; Raffay, M.; Justice, Q.; Al Tamimi, Z.; Hansotte, G.; Sunkara, L. D.; Bernat, J. Additive Manufacturing: A Comprehensive Review. *Sensors* **2024**, 2668.

(26) Zhang, X.; Liou, F.*Introduction to Additive Manufacturing*. Elsevier, In Additive manufacturing, 2021; pp 1−31.

(27) Jaziri, N.; Boughamoura, A.; Müller, J.; Mezghani, B.; Tounsi, F.; Ismail, M. A Comprehensive Review of Thermoelectric Generators: Technologies and Common Applications. *Energy reports* **2020**, *6*, 264−287.

(28) Attene, M. As-Exact-as-Possible Repair of Unprintable STL Files. *Rapid Prototyp. J.* **2018**, *24* (5), 855−864.

(29) Gibson, I.; Rosen, D. W.; Stucker, B.; Khorasani, M.; Rosen, D.; Stucker, B.; Khorasani, M.*Additive Manufacturing Technologies*; Springer, **2021**; Vol. *17*.

(30) Zhang, D.; Sia, S. A.; Solco, S. F. D.; Xu, J.; *Suwardi*; A. Energy Harvesting through Thermoelectrics: Topological Designs and Materials Jetting Technology. 2023.

(31) Leonov, V. Thermoelectric Energy Harvesting of Human Body Heat for Wearable Sensors. *IEEE Sens. J.* **2013**, *13* (6), 2284−2291.

(32) Thimont, Y.; Coderch, A. M.; Chevallier, G.; Duployer, B.; Galodé, A.; Gascoin, F.; Berthebaud, D.; Presmanes, L. Elaboration of P-Type Ge Doped MnSiy (1.73< Y< 1.77) Thermoelectric Legs with Complex Shapes by Binder Jetting Additive Manufacturing Technique. *Acta Mater.* **2025**, *282*, No. 120466.

(33) Du, Y.; Xu, J.; Paul, B.; Eklund, P. Flexible Thermoelectric Materials and Devices. *Appl. Mater. Today* **2018**, *12*, 366−388.

(34) Ou, C.; Sangle, A. L.; Datta, A.; Jing, Q.; Busolo, T.; Chalklen, T.; Narayan, V.; Kar-Narayan, S. Fully Printed Organic−Inorganic Nanocomposites for Flexible Thermoelectric Applications. *ACS Appl. Mater. Interfaces* **2018**, *10* (23), 19580−19587.

(35) Jiao, F.; Di, C.; Sun, Y.; Sheng, P.; Xu, W.; Zhu, D. Inkjet-Printed Flexible Organic Thin-Film Thermoelectric Devices Based on p-and n-Type Poly (Metal 1, 1, 2, 2-Ethenetetrathiolate) s/Polymer Composites through Ball-Milling. *Philosophical Transactions of the Royal Society A: Mathematical, Physical and Engineering Sciences* **2014**, *372* (2013), 20130008.

(36) Zhang, D.; Lim, W. Y. S.; Duran, S. S. F.; Loh, X. J.; Suwardi, A. Additive Manufacturing of Thermoelectrics: Emerging Trends and Outlook. *ACS Energy Lett.* **2022**, *11*, 720−735.

(37) Bi, J.; Liu, Z.; Li, B.; Li, S.; Yang, Z.; Starostenkov, M. D.; Dong, G. Additive Manufacturing of Thermoelectric Materials: Materials, Synthesis and Manufacturing: A Review. *J. Mater. Sci.* **2024**, *59*, 359−381. Springer January 1

(38) Rani, P.; Deshmukh, K.; Kesarla, M. K.; Kar, T.; Pasha, S. K.*Applications of Additive Manufacturing Techniques in the Fabrication of Thermoelectric Materials and Devices*; John Wiley & Sons, Ltd, 2023.

(39) Baroutaji, A.; Arjunan, A.; Robinson, J.; Ramadan, M.; Abdelkareem, M. A.; Vance, A.; Arafat, A.; Olabi, A. G. Developments and Prospects of Additive Manufacturing for Thermoelectric Materials and Technologies. *Sustainable Mater. Technol.* **2024**, *41*, No. e01008.

(40) Wang, J.; Li, H.; Liu, R.; Li, L.; Lin, Y.-H.; Nan, C.-W. Thermoelectric and Mechanical Properties of PLA/Bi0· 5Sb1· 5Te3 Composite Wires Used for 3D Printing. *Compos. Sci. Technol.* **2018**, *157*, 1−9.

(41) Oztan, C.; Ballikaya, S.; Ozgun, U.; Karkkainen, R.; Celik, E. Additive Manufacturing of Thermoelectric Materials via Fused Filament Fabrication. *Appl. Mater. Today* **2019**, *15*, 77−82.

(42) Chen, A.; Madan, D.; Wright, P. K.; Evans, J. W. Dispenser-Printed Planar Thick-Film Thermoelectric Energy Generators. *Journal of Micromechanics and Microengineering* **2011**, *21* (10), No. 104006.

(43) Peng, J.; Witting, I.; Geisendorfer, N.; Wang, M.; Chang, M.; Jakus, A.; Kenel, C.; Yan, X.; Shah, R.; Snyder, G. J.; Grayson, M. 3D Extruded Composite Thermoelectric Threads for Flexible Energy Harvesting. *Nat. Commun.* **2019**, *10* (1), 5590.

(44) Du, Y.; Chen, J.; Meng, Q.; Xu, J.; Paul, B.; Eklund, P. Flexible Ternary Carbon Black/Bi2Te3 Based Alloy/Polylactic Acid Thermoelectric Composites Fabricated by Additive Manufacturing. *Journal of Materiomics* **2020**, *6* (2), 293−299.

(45) Su, N.; Zhu, P.; Pan, Y.; Li, F.; Li, B. 3D-Printing of Shape-Controllable Thermoelectric Devices with Enhanced Output Performance. *Energy* **2020**, *195*, No. 116892.

(46) Choo, S.; Ejaz, F.; Ju, H.; Kim, F.; Lee, J.; Yang, S. E.; Kim, G.; Kim, H.; Jo, S.; Baek, S.; Cho, S.; Kim, K.; Kim, J. Y.; Ahn, S.; Chae, H. G.; Kwon, B.; Son, J. S. Cu2Se-Based Thermoelectric Cellular Architectures for Efficient and Durable Power Generation. *Nat. Commun.* **2021**, *12* (1), 3550.

(47) Kenel, C.; Al Malki, M. M. F.; Dunand, D. C. Microstructure Evolution during Reduction and Sintering of 3D-Extrusion-Printed Bi2O3+ TeO2 Inks to Form Bi2Te3. *Acta Mater.* **2021**, *221*, No. 117422.

(48) Kim, F.; Kwon, B.; Eom, Y.; Lee, J. E.; Park, S.; Jo, S.; Park, S. H.; Kim, B. S.; Im, H. J.; Lee, M. H.; Min, T. S.; Kim, K. T.; Chae, H. G.; King, W. P.; Son, J. S. 3D Printing of Shape-Conformable Thermoelectric Materials Using All-Inorganic Bi2Te3-Based Inks. *Nat. Energy* **2018**, *3* (4), 301−309.

(49) Kim, F.; Yang, S. E.; Ju, H.; Choo, S.; Lee, J.; Kim, G.; Jung, S. h.; Kim, S.; Cha, C.; Kim, K. T.; Ahn, S.; Chae, H. G.; Son, J. S. Direct Ink Writing of Three-Dimensional Thermoelectric Microarchitectures. *Nat. Electron.* **2021**, *4* (8), 579−587.

(50) Lee, J.; Choo, S.; Ju, H.; Hong, J.; Yang, S. E.; Kim, F.; Gu, D. H.; Jang, J.; Kim, G.; Ahn, S.; Lee, J. E.; Kim, S. Y.; Chae, H. G.; Son, J. S. Doping-Induced Viscoelasticity in PbTe Thermoelectric Inks for 3D Printing of Power-Generating Tubes. *Adv. Energy Mater.* **2021**, *11* (20), 2100190.

(51) Yang, S. E.; Kim, F.; Ejaz, F.; Lee, G. S.; Ju, H.; Choo, S.; Lee, J.; Kim, G.; Jung, S. h.; Ahn, S.; Chae, H. G.; Kim, K. T.; Kwon, B.; Son, J. S. Composition-Segmented BiSbTe Thermoelectric Generator Fabricated by Multimaterial 3D Printing. *Nano Energy* **2021**, *81*, No. 105638.

(52) Zhang, D.; Ramiah, J.; Cagirici, M.; Saglik, K.; Solco, S. F. D.; Cao, J.; Xu, J.; Suwardi, A. Thermoelectric Nanowires for Dense 3D Printed Architectures. *Mater. Horiz.* **2024**, *11* (3), 847−854.

(53) Mytafides, C. K.; Wright, W. J.; Gustinvil, R.; Tzounis, L.; Karalis, G.; Paipetis, A. S.; Celik, E. Additive Manufacturing of Highly Conductive Carbon Nanotube Architectures towards Carbon-Based Flexible Thermoelectric Generators. *Energy Advances* **2024**, *3* (7), 1642−1652.

(54) He, M.; Zhao, Y.; Wang, B.; Xi, Q.; Zhou, J.; Liang, Z. 3D Printing Fabrication of Amorphous Thermoelectric Materials with Ultralow Thermal Conductivity. *Small* **2015**, *11* (44), 5889−5894.

(55) Karthikeyan, V.; Surjadi, J. U.; Li, X.; Fan, R.; Theja, V. C. S.; Li, W. J.; Lu, Y.; Roy, V. A. L. Three Dimensional Architected Thermoelectric Devices with High Toughness and Power Conversion Efficiency. *Nat. Commun.* **2023**, *14* (1), 2069.

(56) Shi, J.; Chen, H.; Jia, S.; Wang, W. 3D Printing Fabrication of Porous Bismuth Antimony Telluride and Study of the Thermoelectric Properties. *J. Manuf. Process.* **2019**, *37*, 370−375.

(57) Zhang, H.; Hobbis, D.; Nolas, G. S.; LeBlanc, S. Laser Additive Manufacturing of Powdered Bismuth Telluride. *J. Mater. Res.* **2018**, *33* (23), 4031−4039.

(58) Han, H.; Eun Yang, S.; Lee, J.; Kim, K.; Nam, C.; Jo, S.; Lee, S. H.; Kim, J. Y.; Ahn, S.; Sung Son, J. 3D-Printed Functionally Graded Thermoelectric Materials for Enhanced Power Generation. *Chem. Eng. J.* **2024**, *497*, No. 154547.

(59) Zeng, W.; Tao, X.-M.; Lin, S.; Lee, C.; Shi, D.; Lam, K.; Huang, B.; Wang, Q.; Zhao, Y. Defect-Engineered Reduced Graphene Oxide Sheets with High Electric Conductivity and Controlled Thermal Conductivity for Soft and Flexible Wearable Thermoelectric Generators. *Nano Energy* **2018**, *54*, 163−174.

(60) Li, H.; Mao, P.; Davis, M.; Yu, Z. PEDOT: PSS-Polyethylene Oxide Composites for Stretchable and 3D-Printed Thermoelectric Devices. *Composites Communications* **2021**, *23*, No. 100599.

(61) Kee, S.; Haque, M. A.; Corzo, D.; Alshareef, H. N.; Baran, D. Self-Healing and Stretchable 3D-Printed Organic Thermoelectrics. *Adv. Funct. Mater.* **2019**, *29* (51), 1905426.

(62) Hwang, S.; Jang, D.; Lee, B.; Ryu, Y.; Kwak, J.; Kim, H.; Chung, S. All Direct Ink Writing of 3D Compliant Carbon Thermoelectric Generators for High-Energy Conversion Efficiency. *Adv. Energy Mater.* **2023**, *13* (23), 2204171.

(63) Jung, Y. S.; Jeong, D. H.; Kang, S. B.; Kim, F.; Jeong, M. H.; Lee, K.-S.; Son, J. S.; Baik, J. M.; Kim, J.-S.; Choi, K. J. Wearable Solar Thermoelectric Generator Driven by Unprecedentedly High Temperature Difference. *Nano Energy* **2017**, *40*, 663−672.

(64) Cui, G.-P.; Feng, C.-P.; Xu, S.-C.; Sun, K.-Y.; Ji, J.-C.; Hou, L.; Lan, H.-B.; Shang, H.-J.; Ding, F.-Z. 3D-Printed Bi2Te3-Based Thermoelectric Generators for Energy Harvesting and Temperature Response. *ACS Appl. Mater. Interfaces* **2024**, *16* (27), 35353−35360.

(65) Burton, M. R.; Howells, G.; Mehraban, S.; McGettrick, J. D.; Lavery, N.; Carnie, M. J. Fully 3D Printed Tin Selenide (SnSe) Thermoelectric Generators with Alternating n-Type and p-Type Legs. *ACS Appl. Energy Mater.* **2023**, *6* (10), 5498−5507.

(66) Zhan, R.; Lyu, J.; Yang, D.; Liu, Y.; Hua, S.; Xu, Z.; Wang, C.; Peng, X.; Yan, Y.; Tang, X. Large-Scale SHS Based 3D Printing of High-Performance n-Type BiTeSe: Comprehensive Development from Materials to Modules. *Materials Today Physics* **2022**, *24*, No. 100670.

(67) Pourkiaei, S. M.; Ahmadi, M. H.; Sadeghzadeh, M.; Moosavi, S.; Pourfayaz, F.; Chen, L.; Pour Yazdi, M. A.; Kumar, R. Thermoelectric Cooler and Thermoelectric Generator Devices: A Review of Present and Potential Applications. *Model. Mater. Energy* **2019**, *186*, No. 115849.

(68) Kondaguli, R. S.; Malaji, P. V. Geometry Design and Performance Evaluation of Thermoelectric Generator. *Eur. Phys. J. Spec. Top.* **2022**, *231* (8), 1587−1597.

(69) Thimont, Y.; LeBlanc, S. The Impact of Thermoelectric Leg Geometries on Thermal Resistance and Power Output. *J. Appl. Phys.* **2019**, *126* (9), No. 095101.

(70) Sorrentino, R.; Peverini, O. A. Additive Manufacturing: A Key Enabling Technology for next-Generation Microwave and Millimeter-Wave Systems [Point of View]. *Proceedings of the IEEE* **2016**, *104* (7), 1362−1366.

(71) Hull, C. W.Apparatus for Production of Three-Dimensional Objects by Stereolithography. United States Patent, Appl., No.638905, Filed **1984**.

(72) Poudel, B.; Hao, Q.; Ma, Y.; Lan, Y.; Minnich, A.; Yu, B.; Yan, X.; Wang, D.; Muto, A.; Vashaee, D.; Chen, X.; Liu, J.; Dresselhaus, M. S.; Chen, G.; Ren, Z. High-Thermoelectric Performance of Nanostructured Bismuth Antimony Telluride Bulk Alloys. *Science (1979)* **2008**, *320* (5876), 634−638.

(73) Mallick, M. M.; Franke, L.; Rösch, A. G.; Lemmer, U. Shape-Versatile 3D Thermoelectric Generators by Additive Manufacturing. *ACS Energy Lett.* **2021**, *6* (1), 85−91.

(74) Tiwari, L.; Tang, T.; Rong, J.; Shan, W.; Yang, Y.; Li, X. Thermoelectric Material Fabrication Using Mask Image Projection Based Stereolithography Integrated with Hot Pressing. *Journal of Material Science and Technology Research* **2022**, *9* (1), 105−113.

(75) Wang, X.; Jiang, M.; Zhou, Z.; Gou, J.; Hui, D. 3D Printing of Polymer Matrix Composites: A Review and Prospective. *Compos. B Eng.* **2017**, *110*, 442−458.

(76) Katsantonis, S. N.; Tsamis, C. 3D-Printed Lattice Structures for Thermoelectric Devices−a Review. *J. Mater. Chem. A Mater.* **2025**, *13* (34), 27794−27806.

(77) Park, D.; Lee, S.; Kim, J. Enhanced Thermoelectric Performance of UV-Curable Silver (I) Selenide-Based Composite for Energy Harvesting. *Sci. Rep.* **2021**, *11* (1), 16683.

(78) Ferretti, L.; Russo, P.; Passaro, J.; Nanni, F.; D'Ascoli, S.; Fabbrocino, F.; Bragaglia, M. Sustainable Thermoelectric Composites: A Study of Bi2Te3-Filled Biobased Resin. *Materials* **2025**, *18* (15), 3453.

(79) Ayodele, B. E.*Modeling of FDM 3D Printing for Improved Performance*; Texas A&M University-Kingsville, 2015.

(80) Viskadourakis, Z.; Drymiskianaki, A.; Papadakis, V. M.; Ioannou, I.; Kyratsi, T.; Kenanakis, G. Thermoelectric Performance of Mechanically Mixed Bixsb2-Xte3—Abs Composites. *Materials* **2021**, *14* (7), 1706.

(81) Aw, Y. Y.; Yeoh, C. K.; Idris, M. A.; Teh, P. L.; Hamzah, K. A.; Sazali, S. A. Effect of Printing Parameters on Tensile, Dynamic Mechanical, and Thermoelectric Properties of FDM 3D Printed CABS/ZnO Composites. *Materials* **2018**, *11* (4), 466.

(82) Yu, D.; Chi, G.; Mao, X.; Li, M.; Wang, Z.; Xing, C.; Hu, D.; Zhou, Q.; Li, Z.; Li, C.; Deng, Z.; Chen, D.; Song, Z.; He, Z. Volume-Metallization 3D-Printed Polymer Composites. *Adv. Mater.* **2024**, *36* (35), 2403088.

(83) Shi, X.-L.; Zou, J.; Chen, Z.-G. Advanced Thermoelectric Design: From Materials and Structures to Devices. *Chem. Rev.* **2020**, *120* (15), 7399−7515.

(84) Hassan, K.; Nine, M. J.; Tung, T. T.; Stanley, N.; Yap, P. L.; Rastin, H.; Yu, L.; Losic, D. Functional Inks and Extrusion-Based 3D Printing of 2D Materials: A Review of Current Research and Applications. *Nanoscale* **2020**, *12* (37), 19007−19042.

(85) Ying, P.; Jian, Q.; Gong, Y.; Song, T.; Yang, Y.; Geng, Y.; Huang, J.; Sun, R.; Chen, C.; Shen, T.; Li, Y.; Dou, W.; Liang, C.; Liu, Y.; Xiang, D.; Feng, T.; Fei, X.; Zhang, Y.; Song, K.; Zhang, Y.; Wu, H.; Tang, G. Matrix Plainification Leads to High Thermoelectric Performance in Plastic Cu2Se/SnSe Composites. *Nat. Commun.* **2025**, *16* (1), 3305.

https://doi.org/10.1021/acsami.6c04499
ACS Appl. Mater. Interfaces XXXX, XXX, XXX−XXX

(86) Jin Bae, E.; Hun Kang, Y.; Jang, K. S.; Yun Cho, S. Enhancement of Thermoelectric Properties of PEDOT: PSS and Tellurium-PEDOT: PSS Hybrid Composites by Simple Chemical Treatment. *Sci. Rep.* **2016**, *6* (1), 18805.

(87) Choo, S.; Lee, J.; Şişik, B.; Jung, S. J.; Kim, K.; Yang, S. E.; Jo, S.; Nam, C.; Ahn, S.; Lee, H. S.; Chae, H. G.; Kim, S. K.; LeBlanc, S.; Son, J. S. Geometric Design of Cu2Se-Based Thermoelectric Materials for Enhancing Power Generation. *Nat. Energy* **2024**, *1*, 12−1105.

(88) Haile, B. S.; Pal, V.; Pal, T.; Slathia, S.; Jigi, G. M.; Negedu, S. D.; Tiwari, N.; Singh, H.; Joseph, A.; Olu, F. E.; Tiwary, C. S. Direct Ink Writing (3D Printing) of Robust, Highly Efficient, Double-Half-Heusler Thermoelectric High-Entropy Alloy. *Adv. Eng. Mater.* **2025**, *27* (7), 2402283.

(89) Malki, M. M. A.; Snyder, G. J.; Dunand, D. C. Ink Casting and 3D-Extrusion Printing of the Thermoelectric Half-Heusler Alloy Nb1-XCoSb. *Addit. Manuf. Lett.* **2023**, *4*, No. 100113.

(90) Kumar, I.; Peter, J.; Shankar, G.; Pambannan, P.; Suwas, S.; Biswas, R. K.; Mallik, R. C. Role of Nb Vacancies and Sn Substitution in Modulating the Thermoelectric Properties of NbCoSb. *Phys. Rev. B* **2024**, *110* (20), No. 205207.

(91) Stratasys*PolyJet 3D Printers*. **2024**.

(92) Optomec*Optomec Aerosol Jet Technology*. **2024**.

(93) Juntunen, T.; Jussila, H.; Ruoho, M.; Liu, S.; Hu, G.; Albrow-Owen, T.; Ng, L. W. T.; Howe, R. C. T.; Hasan, T.; Sun, Z.; Tittonen, I. Inkjet Printed Large-Area Flexible Few-Layer Graphene Thermoelectrics. *Adv. Funct. Mater.* **2018**, *28* (22), 1800480.

(94) Besganz, A.; Zöllmer, V.; Kun, R.; Pál, E.; Walder, L.; Busse, M. Inkjet Printing as a Flexible Technology for the Deposition of Thermoelectric Composite Structures. *Procedia Technology* **2014**, *15*, 99−106.

(95) Hüsing, N.; Schubert, U. Aerogels—Airy Materials: Chemistry, Structure, and Properties. *Angew. Chem., Int. Ed.* **1998**, *37* (1−2), 22−45.

(96) Ou, C.; Sangle, A. L.; Chalklen, T.; Jing, Q.; Narayan, V.; Kar-Narayan, S. Enhanced Thermoelectric Properties of Flexible Aerosol-Jet Printed Carbon Nanotube-Based Nanocomposites. *APL Mater.* **2018**, *6* (9), No. 096101.

(97) Weinbach, Q.; Thakkar, S. V.; Carvalho, A.; Chaplais, G.; Combet, J.; Constantin, D.; Stein, N.; Collin, D.; Biniek, L. Efficient Control of a Mesoporous Fibrillar PEDOT: PSS Aerogel Structure for Promising Thermoelectric Applications. *Frontiers in Electronic Materials* **2022**, *2*, No. 875856.

(98) Zhang, D.; Lim, X. J. G.; Li, X.; Saglik, K.; Solco, S. F. D.; Tan, X. Y.; Leow, Y.; Zhai, W.; Tan, C. K. I.; Xu, J.; Suwardi, A. 3D-Printed Porous Thermoelectrics for in Situ Energy Harvesting. *ACS Energy Lett.* **2022**, *8* (1), 332−338.

(99) Zeng, M.; Du, Y.; Jiang, Q.; Kempf, N.; Wei, C.; Bimrose, M. V.; Tanvir, A. N. M.; Xu, H.; Chen, J.; Kirsch, D. J.; Martin, J.; Wyatt, B. C.; Hayashi, T.; Saeidi-Javash, M.; Sakaue, H.; Anasori, B.; Jin, L.; McMurtrey, M. D.; Zhang, Y. High-Throughput Printing of Combinatorial Materials from Aerosols. *Nature* **2023**, *617* (7960), 292−298.

(100) Lou, S.; Jiang, X.; Sun, W.; Zeng, W.; Pagani, L.; Scott, P. J. Characterisation Methods for Powder Bed Fusion Processed Surface Topography. *Precis. Eng.* **2019**, *57*, 1−15.

(101) Mueller, B. Additive Manufacturing Technologies−Rapid Prototyping to Direct Digital Manufacturing. *Assembly Automation* **2012**, *32* (2), 378.

(102) Chueh, Y.-H.; Zhang, X.; Ke, J. C.-R.; Li, Q.; Wei, C.; Li, L. Additive Manufacturing of Hybrid Metal/Polymer Objects via Multiple-Material Laser Powder Bed Fusion. *Addit. Manuf.* **2020**, *36*, No. 101465.

(103) Baudry, M.; Savelli, G.; Roux, G. 3D Printing of Bulk Thermoelectric Materials: Laser Powder Bed Fusion of N-Type Silicon Germanium. *Materials Science and Engineering: B* **2023**, *298*, No. 116897.

(104) Bertoli, U. S.*Process-Structure-Properties Relationships in Laser Powder Bed Fusion Additive Manufacturing*; University of California, Irvine, 2018.

(105) Van Elsen, M.; Al-Bender, F.; Kruth, J.-P. Application of Dimensional Analysis to Selective Laser Melting. *Rapid Prototyp. J.* **2008**, *14* (1), 15−22.

(106) Shi, J.; Tong, Z.; Wang, C.; Li, B.; Cao, S.; Hu, Y.; Wang, Z.; Peng, J. Predictable Thermoelectric Performance of Directly Synthesized Bi0. 5Sb1. 5Te3 Using Laser Powder Bed Fusion Additive Manufacturing. *Ceram. Int.* **2024**, *50* (2), 2921−2930.

(107) Oztan, C.; Şişik, B.; Welch, R.; LeBlanc, S. Process-Microstructure Relationship of Laser Processed Thermoelectric Material Bi2Te3. *Front. Electron. Mater.* **2022**, *2*, 1046694.

(108) Welch, R.; Gubisch, S.; Leblanc, S. Nano/Microstructures and Thermoelectric Properties of Silicon Germanium Manufactured Using Laser Powder Bed Fusion. *J. Mater. Process. Technol.* **2025**, *337*, No. 118749.

(109) Qiu, J.; Yan, Y.; Luo, T.; Tang, K.; Yao, L.; Zhang, J.; Zhang, M.; Su, X.; Tan, G.; Xie, H.; Kanatzidis, M. G.; Uher, C.; Tang, X. 3D Printing of Highly Textured Bulk Thermoelectric Materials: Mechanically Robust BiSbTe Alloys with Superior Performance. *Energy Environ. Sci.* **2019**, *12* (10), 3106−3117.

(110) Wu, K.; Yan, Y.; Zhang, J.; Mao, Y.; Xie, H.; Yang, J.; Zhang, Q.; Uher, C.; Tang, X. Preparation of N-Type Bi2Te3 Thermoelectric Materials by Non-Contact Dispenser Printing Combined with Selective Laser Melting. *physica status solidi (RRL)−Rapid Research Letters* **2017**, *11* (6), 1700067.

(111) Yan, Y.; Geng, W.; Qiu, J.; Ke, H.; Luo, C.; Yang, J.; Uher, C.; Tang, X. Thermoelectric Properties of N-Type ZrNiSn Prepared by Rapid Non-Equilibrium Laser Processing. *RSC Adv.* **2018**, *8* (28), 15796−15803.

(112) Zhou, Y. H.; Zhang, Z. H.; Wang, Y. P.; Liu, G.; Zhou, S. Y.; Li, Y. L.; Shen, J.; Yan, M. Selective Laser Melting of Typical Metallic Materials: An Effective Process Prediction Model Developed by Energy Absorption and Consumption Analysis. *Addit. Manuf.* **2019**, *25*, 204−217.

(113) Shi, J.; Chen, X.; Wang, W.; Chen, H. A New Rapid Synthesis of Thermoelectric Sb2Te3 Ingots Using Selective Laser Melting 3D Printing. *Mater. Sci. Semicond. Process.* **2021**, *123*, No. 105551.

(114) El-Desouky, A.; Carter, M.; Mahmoudi, M.; Elwany, A.; LeBlanc, S. Influences of Energy Density on Microstructure and Consolidation of Selective Laser Melted Bismuth Telluride Thermoelectric Powder. *J. Manuf. Process.* **2017**, *25*, 411−417.

(115) Wu, Y.; Sun, K.; Yu, S.; Zuo, L. Modeling the Selective Laser Melting-Based Additive Manufacturing of Thermoelectric Powders. *Addit. Manuf.* **2021**, *37*, No. 101666.

(116) El-Desouky, A.; Carter, M.; Andre, M. A.; Bardet, P. M.; LeBlanc, S. Rapid Processing and Assembly of Semiconductor Thermoelectric Materials for Energy Conversion Devices. *Mater. Lett.* **2016**, *185*, 598−602.

(117) Wang, X.; Jiang, M.; Zhou, Z.; Gou, J.; Hui, D. 3D Printing of Polymer Matrix Composites: A Review and Prospective. *Composites Part B* **2017**, *1*, 442−458.

(118) Luo, Z.; Zhang, H.; Chen, R.; Li, H.; Cheng, F.; Zhang, L.; Liu, J.; Kong, T.; Zhang, Y.; Wang, H. Digital Light Processing 3D Printing for Microfluidic Chips with Enhanced Resolution via Dosing- and Zoning-Controlled Vat Photopolymerization. *Microsyst. Nanoeng.* **2023**, *9* (1), 103.

(119) Gülcan, O.; Günaydın, K.; Tamer, A. The State of the Art of Material Jetting—a Critical Review. *Polymers* **2021**, *2*, 2829.

(120) Joshua, R. J. N.; Raj, S. A.; Hameed Sultan, M. T.; Łukaszewicz, A.; Józwik, J.; Oksiuta, Z.; Dziedzic, K.; Tofil, A.; Shahar, F. S. Powder Bed Fusion 3D Printing in Precision Manufacturing for Biomedical Applications: A Comprehensive Review. *Materials* **2024**, 769.

(121) Zhu, Y.; Newbrook, D. W.; Dai, P.; de Groot, C. H. K.; Huang, R. Artificial Neural Network Enabled Accurate Geometrical Design and Optimisation of Thermoelectric Generator. *Appl. Energy* **2022**, *305*, 117800.

(122) Vipin, K. E.; Padhan, P. Machine-Learning Guided Prediction of Thermoelectric Properties of Topological Insulator $Bi_2Te_{3-x}Se_x$. *J. Mater. Chem. C Mater.* **2024**, *12* (20), 7415−7425.

(123) Florenciano, I.; Tortosa-Martinez, S.; Molina-Lopez, F. Machine Learning-Driven Optimization of Thermoelectric Materials Laser-Printed on Flexible Substrate. *Adv. Mater. Technol.* **2026**.

(124) Song, K.; Xu, G.; Tanvir, A. N. M.; Wang, K.; Bappy, M. O.; Yang, H.; Shang, W.; Zhou, L.; Dowling, A. W.; Luo, T.; Zhang, Y. Machine Learning-Assisted 3D Printing of Thermoelectric Materials of Ultrahigh Performances at Room Temperature. *J. Mater. Chem. A Mater.* **2024**, *12* (32), 21243−21251.

(125) Headley, C. V.; Herrera del Valle, R. J.; Ma, J.; Balachandran, P.; Ponnambalam, V.; LeBlanc, S.; Kirsch, D.; Martin, J. B. The Development of an Augmented Machine Learning Approach for the Additive Manufacturing of Thermoelectric Materials. *J. Manuf. Process.* **2024**, *116*, 165−175.

https://doi.org/10.1021/acsami.6c04499